PROPERTIES OF BLOCK-COPOLYMER INTERFACES

A Dissertation
Submitted to the Graduate Faculty
of the
North Dakota State University
of Agriculture and Applied Science

By

Damith Pasindu Rozairo

In Partial Fulfillment of the Requirements
for the Degree of
DOCTOR OF PHILOSOPHY

Major Program:
Materials and Nanotechnology

May 2016

Fargo, North Dakota

North Dakota State University
Graduate School

Title

Properties of Block-Copolymer Interfaces

By

Damith Pasindu Rozairo

The Supervisory Committee certifies that this **_disquisition_** complies with North Dakota

State University's regulations and meets the accepted standards for the degree of

DOCTOR OF PHILOSOPHY

SUPERVISORY COMMITTEE:

Dr. Andrew Croll

Chair

Dr. Erik Hobbie

Dr. Sylvio May

Dr. Xinnan Wang

Approved:

05/06/2016	Erik Hobbie
Date	Department Chair

ABSTRACT

There is considerable interest in the fabrication and mechanism of soft spheres and capsules because of their use in a large number of applications ranging from targeted drug delivery systems to cosmetically active agents. The performance of these soft spheres depends on the enhancement of the mechanical properties of these materials. This dissertation is focused on studying the fundamental physics of these soft spheres.

First, we study a simple fluid-fluid system covered by a diblock copolymer. Specifically, we use laser confocal microscopy to adapt a sessile drop geometry to a measurement of the static properties of an ensemble of polystyrene-b-poly(ethylene oxide) (PS-PEO) stabilized oil droplets. We present a simple model derived from Bashforth-Adams model for sessile drops. This method can be used to measure the surface tension of any fluid-fluid interface using a simple optical microscope without looking at the full geometry of a deformed droplet. We then synthesize a polystyrene-b-poly(acrylic acid)-b-polystyrene (PS-PAA-PS) elastic-shell-coated emulsion drop that shows an identical deformation to the fluid-like PS-PEO droplets. Both systems, in sessile geometry, can be related to their basic material properties through appropriate modeling. We find that the elastic shell is dominated by its surface tension, easily enabling it to match the static response of a purely fluid drop.

Motivated by the sessile drop geometry, we study how these idealized cargo carrying spheres interact with a hard wall. As a polymer covered droplet approaches a flat wall, it buckles in and traps an amount of the outer fluid. This fluid is slowly drained out through a narrow channel covered with a polymer brush. A simple scaling model predicts the drainage rate of the fluid through the polymer brush.

Finally, we look at how a long diblock copolymer (PS-PEO) molecule is packed at an oil-water interface and how it affects the surface tension. We find that as the polymer to oil concentration is reduced, it goes from the critical concentration at which no more chains can be fitted to the bare oil interface quickly. Furthermore, we find that the outer brush thickness (PEO) increases as the PS-PEO concentration is increased.

ACKNOWLEDGEMENTS

DEDICATION

To my brother,

Yohan Rozairo

Without whom I would not be where I am today. He has guided me throughout my life, taught

me not to take the easy way out, and that there is no happiness without sorrow. I am forever

grateful to him.

TABLE OF CONTENTS

LIST OF TABLES

LIST OF FIGURES

1. INTRODUCTION

1.1. Research Motivation

Polymers are widely used in industries ranging from food and medical, to coatings and consumables. In recent years, the medical industry has shown interest in using polymers to create advanced drug delivering devices. Typically, polymers are used to create polymersomes, analogous to liposomes which are natural encapsulation systems used to transport cargo inside liquid cells. However, use of the polymer technology remains limited, in part due to the lack of fundamental understanding of polymers at fluid-fluid interfaces. Therefore, it is important to increase the basic understanding of the physics of polymersomes and polymers at fluid interfaces.

1.2. Research Outline

The purpose of this dissertation is to study the static and dynamic properties of block copolymer stabilized emulsion droplets. There are four experimentally investigated projects discussed in this thesis: 1) properties of fluid-like polymer interfaces; 2) synthesis of elastic shells and properties of elastic interfaces; 3) influence of block copolymer in late stage drop drainage; and 4) the packing of block copolymer at emulsion drop interfaces. Preceding this, chapter one consists of a brief introduction to the background physics and chemistry of polymers, capillarity, wetting and fluid mechanics.

Chapter two discusses the interfacial properties of block copolymer stabilized oil emulsions in water. Here, an old method of measuring surface tension, the sessile drop method is developed into an easily used technique. The motivation of this work is that there are few techniques of measuring surface properties of fluid-like interfaces. Here, the term 'fluid-like' is used as the interface between two fluids covered with polymer molecules may not still be considered a fluid interface. Some of the most common techniques used with fluid-like interfaces are the pendent

drop method, the micropipette aspiration method, the Wilhelmy plate method and the sessile drop method. There are drawbacks to each of these techniques and are described in chapter two. For purposes explained in chapter two, we use the sessile drop technique. Traditionally, three dimensional images of fluid drops are required to use the sessile drop method. We use laser scanning confocal microscopy to acquire high quality shape measurements near the contact line using interferometry and use optical sectioning to acquire information far from the contact line. In chapter two, we show how this method can be simplified so that only a simple optical microscope is necessary. Specifically, we use the amphiphilic diblock copolymer polystyrene-b-polyethylene oxide (PS-PEO) to cover an oil droplet in water and measure surface tension. To show the sensitivity of the technique, we measure interfacial properties of oil drops covered with a series of different sized chains.

In chapter three, we investigate the surface properties of elastic interfaces. Motivated by advanced targeted drug delivery systems, we present a novel technique to synthesize elastic shells filled with an incompressible fluid. The motivation behind an elastic interface is to harness the fast responsiveness of elastic instabilities. The elastic membrane was carefully designed to match the interfacial properties of a fluid-like interface. Specifically, we use the triblock copolymer polystyrene-b- polyacrylic(acid)-b- polystyrene to create an elastic shell. Motivated by the work in the previous chapter, a sessile drop technique was employed to measure the surface properties. Both a scaling theory and a full mechanical model are used to describe the properties of the elastic shells.

The work in chapter two and chapter three was focused on studying the static properties of block copolymer coated sessile droplets. In chapter four, we look at the dynamic properties of sessile droplets. This work is motivated by the dynamics of advanced drug delivery systems. The

spherical cargo carriers are bound to interact with other surfaces inside blood vessels and cells. Therefore, it is imperative to understand how these materials approach and equilibrate against walls. We conduct an idealized experiment, where we float a sessile droplet with a brushy diblock copolymer at the drop surface and investigate how it interacts with a mica substrate. Similarly to the emulsion droplets in chapter 2, we use PS-PEO covered oil droplets in water. As the drop approach the mica surface the drop buckles in and traps an amount of water between the droplet and the wall. Thereafter, the trapped water is slowly drained out through a narrow gap created by the self-assembled polymer brush. We investigate how the length of the diblock copolymer affects the drainage rate. We show how a simple scaling model can be used to understand the flow rate.

Motivated by the work done in the earlier chapters, we study the molecular details of polymer stabilized emulsion droplets in the fifth and the last chapter. Specifically we look at how the packing density of the self-assembled diblock copolymer influence the surface tension of the oil-water interface. We use the same diblock copolymer PS-PEO as used in earlier chapters to cover an oil droplet in water to study how the chains are packed at the interface. We find that the critical polymer concentrations needed to fully pack the interface is much smaller for longer polymer chains. Furthermore, we investigate how the packing structure of the diblock copolymer is influencing the thickness of the brushy layer. We show that the self-assembled chains reach a critical polymer density at the interface much more rapidly than small surfactant molecules which ultimately influences the brush thickness and drainage dynamics.

1.3. Polymers

A polymer is a long molecule consisting of many covalently bonded small molecules which are called monomers. The two words polymer and monomer are derived from the ancient Greek words monos- (one), polus- (many) and -meros (part). Polymers are commonly referred to as long chains because it typically consists of 100s to 1000s of monomers. Polymers can be naturally occurring or synthetically made in a laboratory. The first industrially used polymers were modifications of naturally occurring polymers such as natural rubber, although the molecular structure of these materials were unknown at the time. Some of the other polymers in Nature are DNA, cellulose and proteins. Commonly used synthetic polymers include polystyrene (PS, in cups and plates), polyvinyl chloride (PVC, in pipes), nylon (in textiles) and teflon (in non-stick pans). The large molecular weight in polymers compared to small molecule counterparts, gives rise to unique properties and abilities such as viscoelasticity, increased toughness and glass formation.

$$CH_2 = \overset{\overset{R}{|}}{CH} \xrightarrow{\text{INITIATION}} CH_2 - \overset{\overset{R}{|}}{\underset{\underset{H}{|}}{C^*}} \tag{1}$$

$$CH_2 - \overset{\overset{R}{|}}{\underset{\underset{H}{|}}{C^*}} + n\ CH_2 = \overset{\overset{R}{|}}{CH} \longrightarrow \left[CH_2 - \overset{\overset{R}{|}}{\underset{\underset{H}{|}}{C}} \right]_n CH_2 - \overset{\overset{R}{|}}{\underset{\underset{H}{|}}{C^*}} \tag{2}$$

$$\left[CH_2 - \overset{\overset{R}{|}}{\underset{\underset{H}{|}}{C}} \right]_n CH_2 - \overset{\overset{R}{|}}{\underset{\underset{H}{|}}{C^*}} \xrightarrow{\text{TERMINATION}} \left[CH_2 - \overset{\overset{R}{|}}{\underset{\underset{H}{|}}{C}} \right]_n CH_2 - \overset{\overset{R}{|}}{\underset{\underset{H}{|}}{C}} - T \tag{3}$$
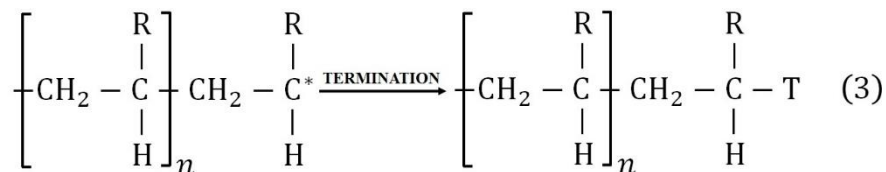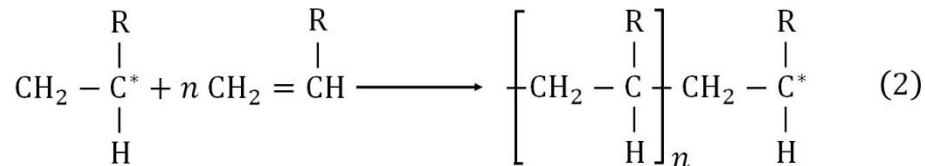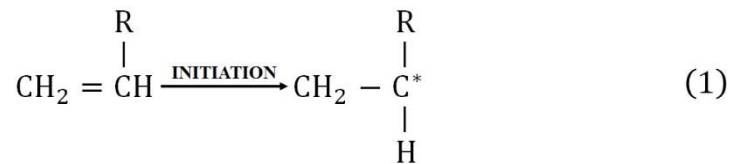
Figure 1.1. Three step addition polymerization method for ethane with a functional group R. Steps are as follows; (1) initiation, (2) chain propagation and (3) chain termination.

Polymerization is the process by which monomers[1] are chemically combined with each other. There are three general types of monomers utilized in polymer synthesis: 1) a monomer consisting of double or triple bonds that can undergo further reactions to connect monomers; 2) molecules which contains two functional end groups that allows condensation reactions; and 3) cyclic compounds that undergo ring-opening polymerization. Addition polymerization is the most common method for synthesizing macromolecules. As shown in figure 1.1, in this technique the overall polymerization mechanism can be described in 4 simple steps, initiation, chain propagation, chain termination and chain transfer. The first step is the process in which a reactive species initiates the polymerization by unsaturation a monomer. Next, the activated monomer connects to an unactivated monomer to create a dimer and the process repeats. The reaction is terminated by the addition of a third molecule which bonds to the growing chain but does not allow subsequent growth.
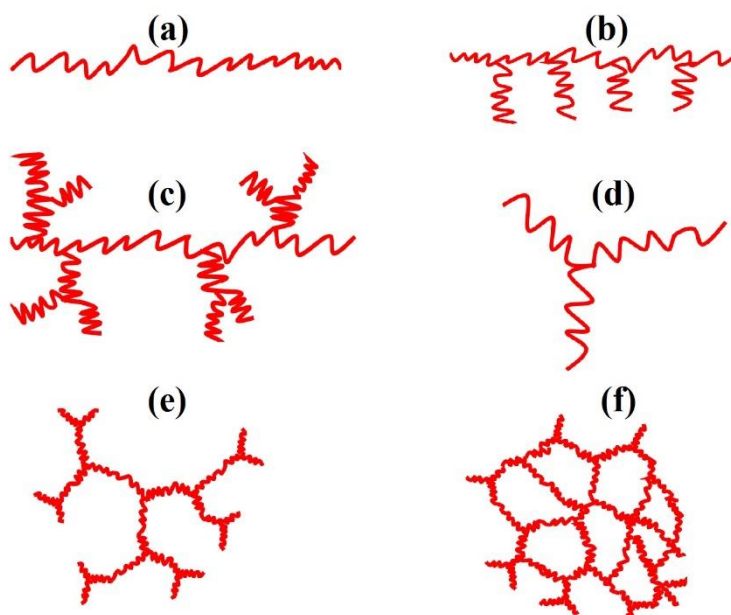
Figure 1.2. Different types of homopolymer architectures: (a) linear, (b) comb, (c) branched, (d) star, (e) dendritic and (f) crosslinked.

There are several different classifications of polymers. One type is based on the structure of the skeleton and the architecture of the polymer chain. Some common types of architectures are linear, comb, branched, star, dendritic and crosslinked (see figure 1.2). The architecture of the polymer can change the properties such as viscosity, rigidity, thermal stability and crystallization. For example, linear extended chains are soluble in an appropriate solvent. This solution has a higher viscosity than the bare solvent owing to their polymer chain entanglements. Similarly, combs, dendrimers and crosslinked polymer have higher viscosities in solution. Polymers can also be synthesized using a mixture of different monomers and these are called copolymers. Examples of this category are linear block copolymer, comb copolymer and dendrimetric copolymer. It is advantageous to synthesize copolymers according to the need of specific applications. Examples of different types of copolymers (according to its architecture) are depicted in figure 1.3
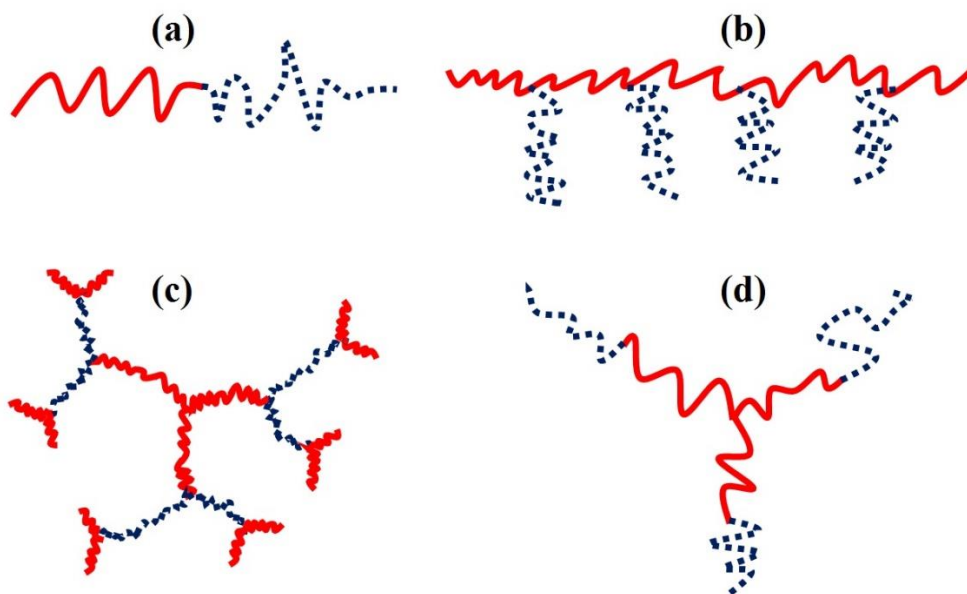
Figure 1.3. Different types of block copolymer architecture: (a) linear diblock copolymer, (b) comb copolymer, (c) dendrimetric copolymer and (d) star copolymer.

The concepts of polymer physics were heavily studied between the years of 1930 and 1960. Polymer synthesis methods and polymer behavior in different solvents were well established by a few important scientists, namely, Warner Kuhn (1899-1963), Paul Flory (1910-1958), Maurice Huggins (1897-1981). Kuhn's work included defining the size of macromolecules, Flory's work included a single chain swelling, Flory and Huggins established the thermodynamic properties of polymers and phase behavior. Modern polymer physics was well established by Pierre de Gennes (1932-2007) who introduced scaling concepts in polymer physics. A brief introduction to statistical physics of polymer is provided in the following subsections.

1.3.1. Polymer Statistics

As discussed above polymerization is the process in which monomers are covalently bonded together, creating large macromolecules. A common feature in most synthetic polymers are that they are polydisperse, meaning, each chain differ in size. If a sample of polymer has chains with the same number of monomers the sample is called monodisperse. Although this is common in natural polymers such as proteins, monodisperse samples are very rare among synthetic polymers [2,3]. A sample of synthetic polymer consists of individual chains with distribution of degree of polymerization. The molar mass M of a monodisperse sample of polymer with a degree of polymerization of N and monomer molar mass of M_{mon} is given as $M = NM_{mon}$. This is not an ideal way to calculate the molar mass of a polymer as samples are rarely monodisperse. Therefore, it is more accurate to describe the molar mass of a polymer using the number average molecular weight M_n and the weight average molecular weight M_w. These are defined as

$$M_n = \frac{\sum_i N_i M_i}{\sum_i N_i}$$

$$M_w = \sum_i \left[\frac{(N_i M_i)^2}{\sum_i N_i M_i} \right]. \tag{1.1}$$

The polydispersity index (PDI) is defined as the ratio of the weight average and number average molecular weights M_w/M_n. A monodisperse sample will have a PDI of 1 as $M_w = M_n$, while higher PDI corresponds to a broader distribution of chain sizes in the sample.

Over the years, several different models have been presented to describe the static conformation of ideal polymer chains and real polymer chains. Here, the most commonly used models are briefly discussed, namely, a simple random walk (freely rotating chain), self-avoiding random walk and Flory's contribution.

1.3.2. Simple Random Walk

A random walk is one of the simplest idealizations of a polymer chain. It can be described using a periodic lattice where each step in the random walk is a point in the lattice. The walk is defined by taking N steps where each step has the same probability of landing on any of the nearest neighboring points. The length of each step or the size between two points in the lattice is a. If each point has z neighbors, the total number of possible steps is z^N. The end-to- end vector $\boldsymbol{r}$ is addition of all the step vectors of length a ($\sum_n a_n$). Since different $\boldsymbol{a}$ vectors have completely independent orientations, the average square end-to-end distance $\langle r^2 \rangle = \sum_{nm} \langle \boldsymbol{a_n} . \boldsymbol{a_m} \rangle = Na^2$. Qualitatively, we can define the end-to-end distance of a random walk as $\boldsymbol{R_o} = a\sqrt{N}$.

Another way in which a polymer chain can be described is by using the Kuhn length, named after Werner Kuhn. Kuhn segment length is the characteristic length of a polymer in which the segment is freely jointed without consideration of any bond angles, torsion angles and bond lengths similarly to the random walk model. The length of a fully extended Kuhn segment chain is $L = Na$ and the end-to-end distance of it is same as the random walk model ($\boldsymbol{R_o} = a\sqrt{N}$).

1.3.3. Self-Avoiding Random Walk and Flory's Theory

In the previous section the conformation of a polymer chain was explained using simple random walk in an idealized setting where the monomer-monomer interactions were ignored. Here, the conformation of a real polymer chain with monomer-monomer interactions qualitatively described. Consider the energy potential $U(r)$ of bringing two monomers to within a distance of r. This kind of a potential can be described by a Lennard-Jones potential which is shown in figure 1.4(a). The first part of the potential corresponds to the monomer-monomer hard-core repulsion of the two overlapping monomers. A similar interaction will occur with solvent. Figure 1.4(b) shows a hard-core potential, which represents the case where a monomer is chemically identical to solvent molecules. There is no attraction or repulsion between the solvent and the monomer, only a monomer-monomer hard-core repulsion.
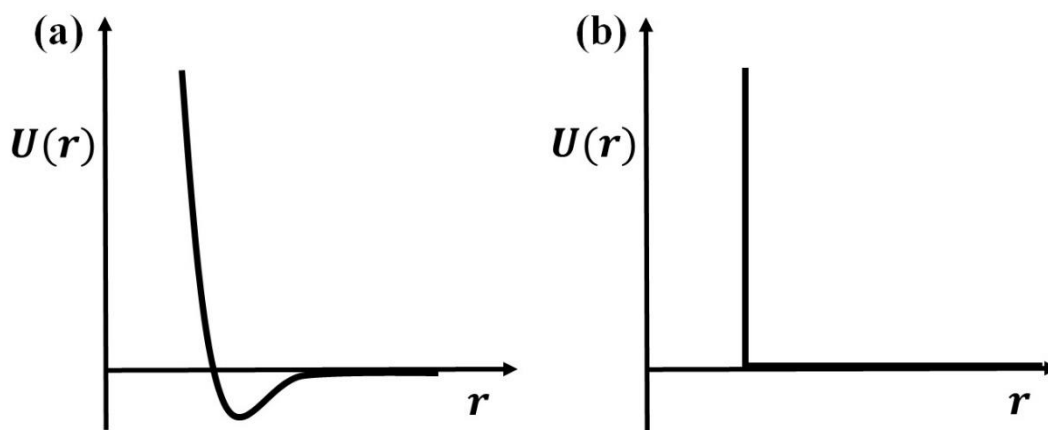
Figure 1.4. (a) The effective interaction potential between two monomers in a solution of other molecules. (b) The hard-core potential preventing two monomers from overlapping. (Adapted from [2])

A self-avoiding polymer chain can be described statistically using the probability of two monomers separated by a distance r. The probability in a chemically different solvent at a temperature T will be proportional to the Boltzmann factor $e^{-U(r)/K_B T}$. Henceforth, the statistical position of the polymer chain can be numerically calculated using: (i) Exact counting of walks for

finite number of steps ($N\sim10$) and extrapolating or (ii) Computer generated Monte Carlo simulations [4].

In the previous section, the end-to-end distance for the simple random walk was found to be $R_o = aN^{1/2}$. The end-to-end distance for a real chain can be described as $R = aN^\nu$ and a real chain is much larger than an ideal chain. We can estimate this exponent ν to remarkable accuracy due to Flory's theory. Here, his theory and the approximations are briefly described. The monomer concentration for a chain with N segments and a certain radius R is

$$c \sim \frac{N}{R^3}. \tag{1.2}$$

Flory approximated the total free energy F of a real polymer chain to be the sum of the repulsion energy R_{rep} due to the excluded volume and the entropic energy R_{el}. If each monomer occupies a volume v ($\sim a^3$) which is excluded to other monomers, the free energy due repulsion can be described as

$$F_{rep} \cong K_B T v \frac{N^2}{R^3} \tag{1.3}$$

This provides the energy of the chain to be stretched as each monomer is repulsed. The expansion is opposed by the entropic energy of the chain. This gives the elastic component of the total free energy as

$$F_{el} \cong K_B T \frac{R^2}{Na^2}. \tag{1.4}$$

Combining equation 1.3 and 1.4 gives us the total free energy of a chain as

$$\frac{F}{K_B T} \cong \frac{a^3 N^2}{R^3} + \frac{R^2}{Na^2} \tag{1.5}$$

Minimizing the free energy of a chain with respect to R ($\partial F / \partial R = 0$) gives the size of a real chain according to the Flory theory:

$$R_F \sim aN^{3/5}.$$ (1.6)

This exponent $3/5$ is remarkably very close to the actual value 0.588 [4] which has been calculated using above mentioned computer simulations.

1.4. Capillarity and Wetting

Capillary action is a physical phenomenon which is a result of surface, or interfacial properties. Particularly with fluids which have deformable surfaces that can change shape in order to minimize the surface energy. Examples of these types of interfaces are a surface between air and liquid or a surface between two immiscible liquids. The phenomenon was first studied by Pierre Simon de Laplace (1749-1827) and Thomas Young (1773-1829) in the early 19th century. Capillary actions are useful in a number of fields ranging from plant biology and surface physics to glass and textile industries. The study of capillarity provides the basic understanding needed to describe the concavity of the surface of water (meniscus) in a graduated cylinder and to understand the differences in shape between a water droplet on a piece of paper vs. a lotus leaf.

1.4.1. Surface Tension

Surface tension is a distinctive property of liquids. It is the property which allows small insects to walk or stride on the surface of water. A liquid is a condensed material which takes the shape of its container. The molecules in a liquid attract each other enough to beat the thermal energy (entropy) and form a denser phase than gas. A liquid molecule surrounded by other liquid molecules has an energy proportional to the number of neighbors, whereas, a liquid molecule at the surface has roughly half the cohesive attractions. This drives the liquid to minimize the surface area exposed by changing its shape. The cohesive attraction between molecules give rise to the property known as 'surface tension'.

As one would expect, the surface tension changes at different temperatures as thermal agitation allows liquid molecules to move around more freely. The surface tension is typically tabulated for interfaces with two surfaces interacting rather than for an individual liquid. For example, water-helium has a higher surface tension than water-toluene. The surface tension can also be defined as the cohesion energy of liquid molecules per surface area [5]. Most oils are held together by van der Waals type interactions, hence, the energy U is comparable to thermal energy ($K_B T$) and at $20^0 C$ gives a surface energy $\gamma = 20 \ mJ/m^2$. Whereas, water has a surface energy of close to $72 \ mJ/m^2$ due to its stronger hydrogen bonds. γ is the energy required to increase the surface area by one unit [5]. Dimensionally, the surface tension can also be written as force per unit length. Typically, the surface tension is expressed in mN/m which is dimensionally equivalent to mJ/m^2. It is important to note that certain types of polymer have the ability to reduce the surface tension of a liquid interface. This will be discussed in detail in chapter two.

1.4.2. Laplace Pressure

The Laplace pressure is the pressure difference between two sides of a curved interface. For example, the pressure difference between the inside and the outside of a droplet or a bubble. The Laplace pressure is caused by the surface tension of the interface and the curvature of the surface. As the radius of the curved surface is increased the Laplace pressure is decreased. For example, the Laplace pressure of a large bubble is lower than that of a smaller bubble with the same surface tension [5].
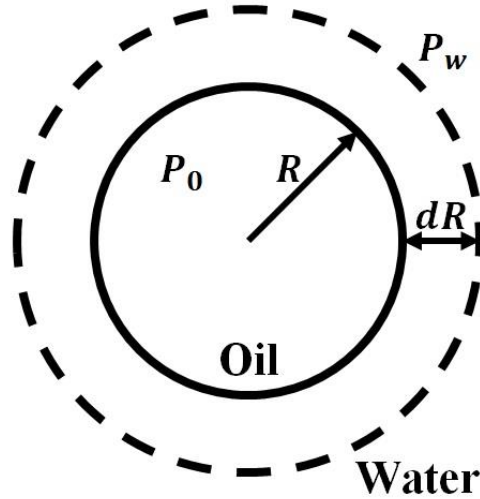
Figure 1.5. A schematic representation of a droplet (with a surface tension of γ) expanding the volume.

The precise Laplace pressure of a spherical bubble or a droplet can be calculated as follows. An oil droplet (of radius R) in water adopts a spherical shape to minimize the surface energy by minimizing the surface area exposed at the interface as shown in figure 1.5. The work done δW for increasing the drop size by dR can be written as

$$\delta W = \gamma \, dA - P_0 \, dV_0 - P_w dV_w \tag{1.7}$$

where γ is the surface tension between water, dA is the increase in surface area of the sphere, dV_o and dV_w are the change in volume of oil and water and P_0 and P_w are the pressures in the oil and the water respectively. The change in volume of the oil and change in volume of water is $dV_0 = -dV_w = 4\pi R^2 \, dR$ and the change in the interfacial area is $dA = 8\pi R \, dR$. Minimizing the work done gives the Laplace pressure:

$$\Delta P = P_0 - P_w = \frac{2\gamma}{R}. \tag{1.8}$$

Similarly, for any curved surface, the Laplace pressure is the product of the surface tension γ and the curvature of the surface κ and commonly written as

13

$$\Delta P = \gamma \kappa = \gamma \left(\frac{1}{R_1} + \frac{1}{R_2} \right), \tag{1.9}$$

where R_1 and R_2 are the two principal radii of curvature of the curved surface.

1.4.3. Wetting

Wetting is the process in which a liquid is deposited on a solid substrate or on an immiscible liquid. The spreading of the liquid is dependent on the balance of surface energies of the three interfaces. Typically, wetting involves three phases; gas, liquid and solid. An important length scale often used in describing wetting phenomenon is the contact angle. The contact angle is conventionally defined as the angle the created by the liquid-gas line meet the substrate (see Figure 1.6). There are three distinctive types of wetting: a) total wetting, b) partial wetting and c) non-wetting. When a drop of water is deposited on a glass surface, the drop may spread, whereas, a water drop on a Teflon surface will ball up to minimize contact.

(a)   **(b)**   **(c)**

Total Wetting   **Partial Wetting**   **Non-Wetting**
$(\theta = 0)$ $(0 < \theta < 90^0)$ $(\theta = 180^0)$
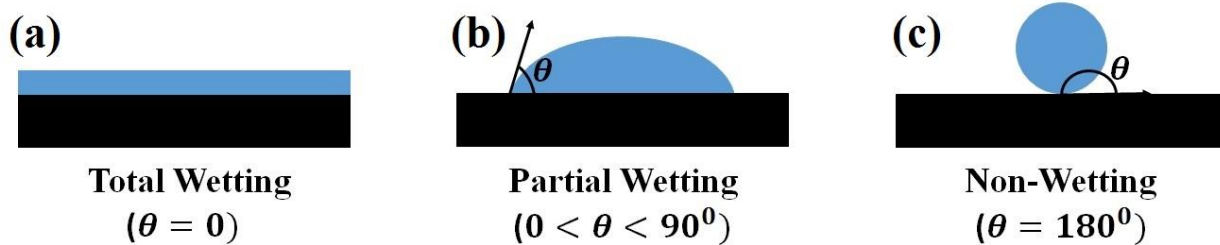
Figure 1.6. Three types of wetting phenomenon: (a) perfectly wetting, (b) partially wetting and (c) non-wetting.

The mechanics of wetting can be understood using the spreading parameter. The spreading parameter, S, is the difference in surface energy between a completely dry surface and a completely wet surface ($S = U_{dry} - U_{wet}$). This can be expressed using the surface tensions of the three interfaces; liquid-gas (γ), solid-liquid (γ_{SL}) and solid-gas (γ_{SG}) as

$$S = \gamma_{SG} - (\gamma_{SL} + \gamma). \tag{1.10}$$

If the spreading parameter is positive ($S > 0$), the liquid completely wets the substrate minimizing

its surface energy. In the opposite case, if $S < 0$, the drop partially wets the substrate creating a

contact angle θ. The contact angle can be calculated by balancing the three forces at the point at

which the three phases meet by projecting the surface tension of each surface on to the substrate

plane (see figure 1.7). This relationship is named as the Young-Dupré equation;

$$\gamma \cos \theta + \gamma_{SL} = \gamma_{SG} \tag{1.11}$$
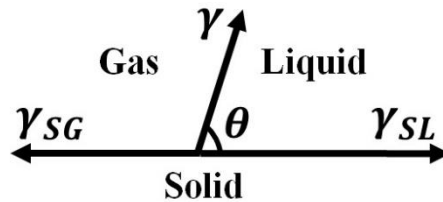
Figure 1.7. Schematic representation of the surface tension at the triple line where a liquid drop
is deposited on a solid substrate in a gaseous environment.

1.5. Fluid Dynamics of Thin Film

Fluid dynamics is the study of the motion of fluids. A fluid can be regarded as a continuous

medium which means it is comprised of small volume elements rather than discrete molecules.

The motion of objects are defined by Newton's second law of motion ($\boldsymbol{F} = m\boldsymbol{a}$). Defining the

motion of fluids quickly becomes a difficult task as this equation has to be applied to each volume

element. For a given body of fluid moving at an average velocity $\boldsymbol{v}$ with a density of ρ for an

incompressible fluid ($\nabla . \boldsymbol{v} = \boldsymbol{0}$), the motion can be described using what is known as the Navier-

Stokes equation [6]:

$$\frac{\partial \boldsymbol{v}}{\partial t} + (\boldsymbol{v} . \nabla)\boldsymbol{v} = -\nabla \left(\frac{P}{\rho}\right) + \eta \nabla^2 \left(\frac{\boldsymbol{v}}{\rho}\right) + g. \tag{1.12}$$

Here, the velocity is a vector in three-dimensional space, g is the gravitational acceleration,

P is the pressure in the system and the second term on the right hand side is viscous term which

opposes any movement due to viscosity η. Luckily, the 1.12 equation can be simplified to what is

15

known as the lubrication approximation when the fluid is confined to a thin region. There are several important outcomes from the approximation. 1) The flow is one dimensional; the velocity of each volume elements point only in one direction. 2) The inertial term which is proportional to v^2 can be neglected compared to the viscous term (proportional to v).
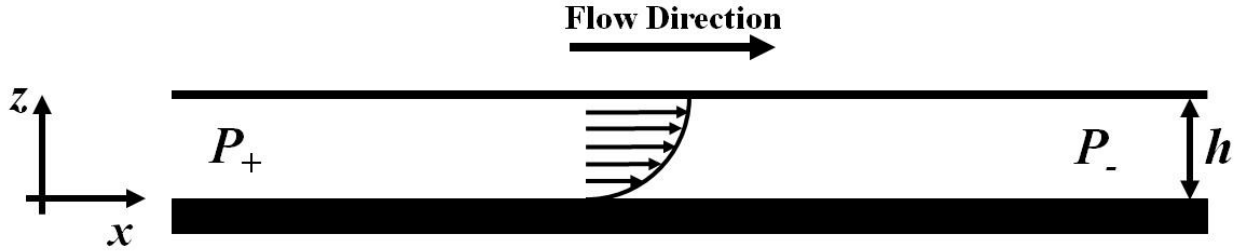
Figure 1.8. A schematic of a liquid flowing from high pressure P_+ to P_-. The arrows inside the fluid depicts the velocity gradient in the z direction.

If the fluid film is flowing along a horizontal flat wall (see figure 1.8) the driving force can be described as a difference in pressure between the two ends. In this case the driving force of the flow would be $P_+ - P_- = \Delta P$. Hence, the Navier-Stokes equation reduces to

$$-\frac{\partial P}{\partial x} + \eta \frac{\partial^2 v}{\partial z^2} = 0. \tag{1.13}$$

Since the driving force is independent of the z axis, the equation can be solved by two successive integrations with respect to z. This gives us a parabolic solution ($v(z) = \alpha_1 z^2 + \alpha_2 z + \alpha_3$) which can be solved using the two boundary conditions (for example, $v(z = 0) = 0$ and $\left.\frac{\partial v}{\partial z}\right|_{z=h} = 0$). This gives the general solution for the average velocity in a thin film as:

$$v(z) = \frac{1}{2\eta} \left(\frac{\partial v}{\partial z}\right) [z^2 - 2zh]. \tag{1.14}$$

16

2. STATIC PROPERTIES OF BLOCK COPOLYMER AT FLUID INTERFACES

2.1. Introduction

Polymers have become an integral part of human life having become indispensable in many industrial applications. One such application is encapsulation, which is used in industries ranging from food and cosmetics to pharmaceutical [7-9]. Encapsulation is attractive as it allows cargo to be isolated and to be delivered to the necessary location. The pharmaceutical industry has made significant investment in adapting amphiphilic block copolymers for use in drug delivery schemes [7,10-12]. A key feature of the technology is a swollen brushy layer on the capsule exterior, often polyethylene oxide (PEO), which creates a very low adhesion surface. The low adhesion is critical to the capsule's ability to evade recognition as a foreign body [13].

The technology remains far from use in part due to the limited understanding of polymers at these interfaces. For example, as an interface is filled with polymer chains, it becomes capable of bearing a shear force. In other words, the interface becomes viscoelastic. In this chapter, we present the experimental procedure, results and discussion of the static properties of block copolymer self-assembled emulsion droplets.

2.1.1. Amphiphiles: Lipids and Block Copolymers

An amphiphile has two parts to it structure. Amphiphilic compounds possess two chemical affinities; 1) a water liking part (hydrophilic) and 2) an oil liking part (hydrophobic or oleophilic) [12]. These can be naturally occurring structures such as phospholipids, cholesterol and fatty acids or synthetic materials such as sodium dodecyl sulfate and certain block copolymers. The most commonly used amphiphiles include soap (or any kind of detergent) and lipoproteins. Chemically, the hydrophilic part is polar and the hydrophobic part is apolar [14]. Typically, the hydrophilic part of the compound would either include an ionic group or a polar group. These groups align in

water as water is a polar molecule whereas, the hydrophobic part contains no polar or ionic groups. The hydrophobic part typically consists of a long hydrocarbon chain with no affinity to water. Phospholipid is a natural amphiphilic compound which helps create bilayer membranes and vesicles. The most widely used industrial application for amphiphilic molecules is the soap and detergent industries.

2.2. Pendant Drop Technique

The pendant drop method is a technique where the geometry of a fluid droplet is used to measure the surface tension. The droplets can either be created as fluid-fluid, fluid in air or air in fluid. The droplet is blown out of a needle with radius r and the weight of the drop is dependent on the surface tension and the size of the needle opening [15-17]. In other words, higher the surface tension or larger the needle opening, heavier the droplet that can be held from the needle. The fundamental physics of the method is described below.
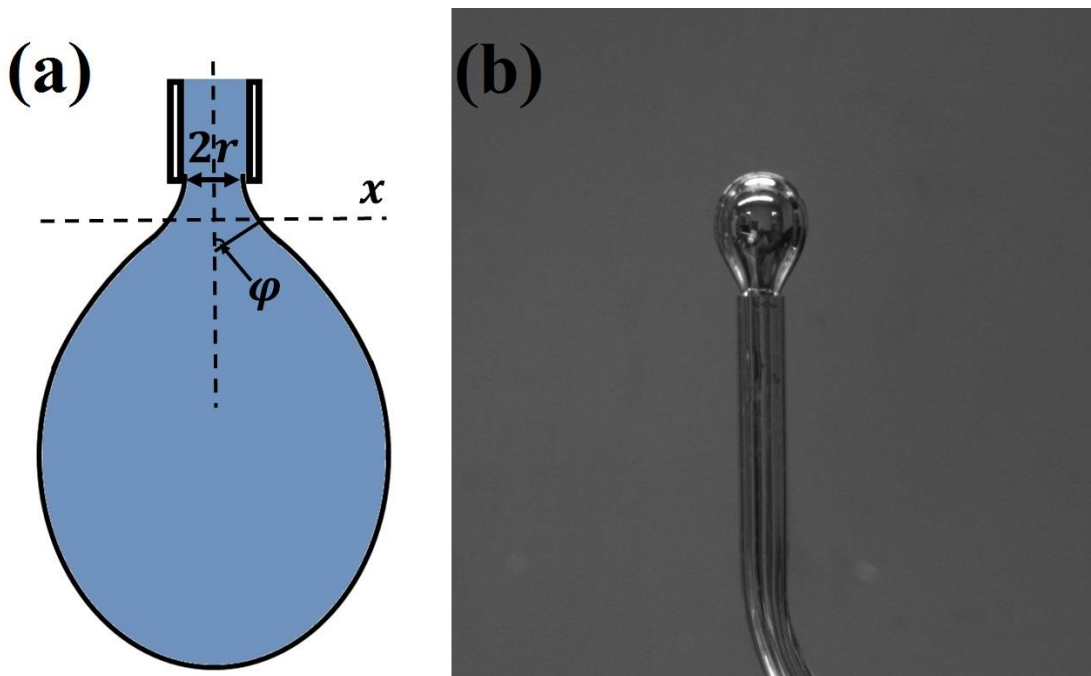
Figure 2.1. (a) Side view schematic of the pendent drop geometry. (b) Experimental micrograph captured using an optical microscope. Upside down air droplet blown out from a glass micropipette in water.

There are two equations relating the geometry and the fundamental physics of the pendant drop. A Laplace pressure is created by the curved surface (equation 2.1) and the balance of the vertical forces acting on a horizontal plane [17-19] (equation 2.2);

$$P = \gamma \left(\frac{1}{R_1} + \frac{1}{R_2} \right) \tag{2.1}$$

$$2\pi x \gamma \sin \varphi = V\rho g + \pi x^2 P. \tag{2.2}$$

P is the pressure created by the surface with the two principal radii of curvature R_1 and R_2 and γ is the surface tension between the inner and the outer fluid. V is the volume of the fluid droplet below the horizontal plane (see figure 2.1 (a)), ρ is the density difference, g is the gravitational acceleration, x is the horizontal position and φ is the angle between the normal to the surface and the z axis. Coupled with geometry and the radius of curvature R_2 being infinite at the point of inflection:

$$\gamma = \frac{g}{\pi} \frac{V\rho R}{x^2}. \tag{2.3}$$

There are several shortcomings to this equation [17]; 1) the inflection plane is a difficult point to find and 2) the volume below this plane is hard to calculate. Therefore, the geometry of the droplet can be used to calculate the surface tension. A detailed derivation of the calculation can be found in the paper by Tucker et al [17]. A similar calculation is derived for the sessile drop method in the section 2.4.

2.3. Micropipette Aspiration Technique

Micropipette aspiration method is a technique developed to calculate the physical properties of red blood cell membranes [20,21]. Specifically, the resistance to deformation due to rigidity and tension in the membrane is measured using this technique. In this section, the technique and the theory behind the measurement is briefly discussed.

Figure 2.2 shows the basic geometry of the experiment. A spherical droplet with a surface tension of γ and a radius of curvature of R produces a Laplace pressure of [19];

$$P_3 - P_2 = \frac{2\gamma}{R}. \tag{2.4}$$

This is the pressure difference across the interface between inner and the outer fluids. As the pressure in the pipette is increased, the projection length L increases and the droplet is aspirated into a micropipette. This creates another curved interface and a Laplace pressure of

$$P_3 - P_1 = \frac{2\gamma}{r}. \tag{2.5}$$

Hence, the difference between equations 2.4 and 2.5 gives the pressure balance in the sphere across all interfaces;

$$P_2 - P_1 = 2\gamma \left(\frac{1}{r} - \frac{1}{R}\right). \tag{2.6}$$

Therefore, if the pipette inner radius, the droplet radius and the micropipette pressure are known (relative to the outer fluid), measuring the surface tension becomes a simple calculation. This is a good method to measure the surface tension of a fluid droplet.

However, there are also many drawbacks of this technique as the droplet is covered with polymers and as the interface goes from fluid to elastic. If the fluid interface is covered with a surfactant or a polymer, the technique demonstrates a time dependent surface tension change as the molecules at the interface are mobile. Furthermore, as the drop surface goes from fluid to elastic, the mechanics of the interface changes considerably. First the drop surface gains the ability to bear a shear force. This introduces a change in volume and change surface area of the spherical part of the droplet [20-23].
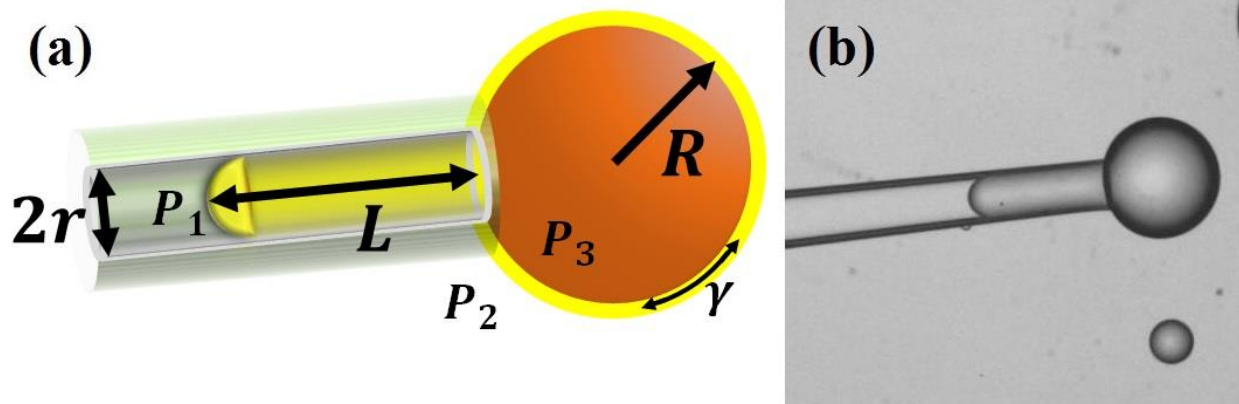
Figure 2.2. (a) Side view schematic of the micropipette aspiration setup. (b) Experimental micrograph captured using an optical microscope. Diblock copolymer covered toluene droplet in water aspirated into a glass micropipette.

2.4. Sessile Drop Theory

There exist many techniques that can be used to measure static properties of fluid interfaces [22,24-29], two of which are discussed in the two preceding sections. However, owing to the broader goal of characterizing both fluid-like and elastic-like interfaces, the sessile drop technique was utilized. Measuring the interfacial properties can be difficult as the interface is changed from fluid to solid. For example, the pendent drop and micropipette aspiration can be used to measure fluid drops but not elastic capsules [30]. In a pendent drop experiment, the weight of the droplet is balanced by the surface tension at the boundary of the nozzle. This allows a simple calculation of the surface tension for a known droplet weight and a nozzle size. The pendent drop works well for fluid interfaces but to measure an elastic interface it requires the surface to be synthesized after the droplet is formed, since this method relies on forming the droplet through the nozzle using a reservoir of the droplet phase.

The micropipette aspiration method relies on balancing the aspiration pressure to the Laplace pressure of the droplet. This works well for a fluid droplet but as the interface becomes elastic, squeezing the droplet into the pipette induces sharp bending which may lead to rupture in

the elastic shell [10]. Therefore, it is beneficial to use a simple sessile drop method which involves no external forces other than the weight of the droplet.

The sessile drop technique is often considered as a technique for measuring surface energies of solid substrates. This is because the contact angle is related to the surface energies. If a drops surface energies (tension) is known, it becomes a simple calculation to measure the substrate surface properties. This was first argued, developed and mathematically proved in the early 1800s by Thomas Young, Pierre-Simon Laplace and Carl Friedrich Gauss [18,19,28]. In 1883, Francis Bashforth and J.C. Adams presented their work on combining the geometry of a sessile droplet under gravity to its surface energies [28]. The most remarkable breakthrough in their work was numerically solving the second order nonlinear differential equation (which describes the shape of the droplet) by hand.

2.4.1. Small Fluid Droplets

A fluid drop can be categorized as small or large. A small droplet has a radius R that is smaller than the capillary length, $\kappa^{-1} = \sqrt{\gamma/\rho g}$, and are dominated by surface forces. The droplet takes on a shape which minimizes its surface area. In isolation the droplet is a sphere, but interaction with a flat substrate causes the drop to take on the shape of a spherical cap with a contact patch of radius r (see figure 2.3). This is due to the dominance of capillary forces over gravity. The size of the contact patch can be determined by balancing the surface forces at the contact line and is given as:

$$r = R \sin \theta, \tag{2.7}$$

with the contact angle given by the well-known Young-Dupré relation (equation 1.11).
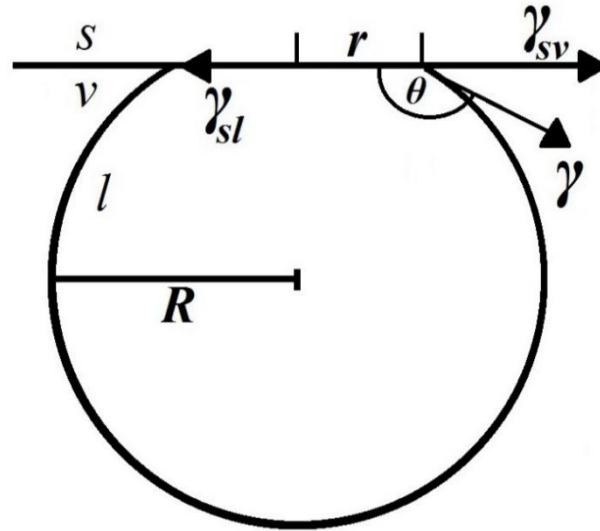
Figure 2.3. Side view schematic of a fluid droplet smaller than the capillary length with a radius R contact angle θ and contact radius r, resting on a solid substrate in a vapor environment.

2.4.2. Large Fluid Droplets

As the size of the drop becomes larger than κ^{-1}, gravity begins to dominate over capillary forces. Therefore, the droplet shape deforms from the ideal spherical shape (see figure 2.2). The additional gravitational pressure does two things, 1.) the contact patch becomes larger non-linearly with the drop size, R, and 2.) the macroscopic contact angle no longer remains constant.
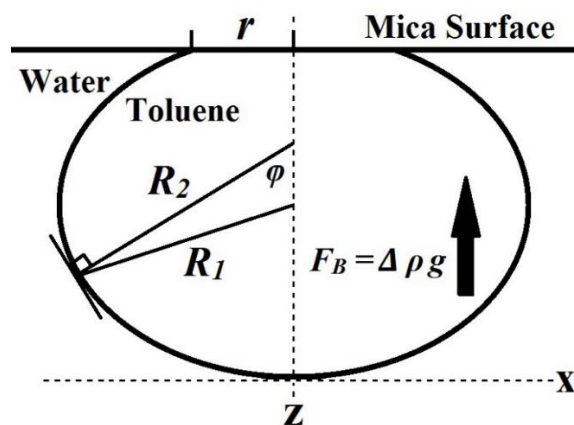
Figure 2.4. Schematic representation of a droplet with principal radii of R_1 and R_2, pushed against a flat substrate.

The deformed drop shape is mathematically defined as following. The droplet has two principal radii R_1, R_2 (see figure 2.4) originating from a point on the drop surface. R_1 rotates around the z axis, R_2 is orthogonal to the drop surface and R_2 creates angle φ with respect to the z-axis and moves in the x-z plane. At any point above the origin, the Laplace pressure due to the curved droplet interface is equal to the hydrostatic pressure at that point,

$$\gamma_1 \kappa_1 + \gamma_2 \kappa_2 = p_0 + \rho g z, \tag{2.8}$$

where γ is a tension, κ is a curvature and the subscripts refer to the two principal radii of curvature. The hydrostatic pressure has a maximum at the drop apex (the lowest point in our inverted geometry) and decreases in proportion to distance from the droplet apex, z, the difference in density between the interior and exterior fluids, ρ, and the gravitational acceleration, g. The minimum at the apex can be related to the curvature at this point, $1/b$, (where $R_1 = R_2 = b$) through the Laplace pressure, $p_0 = \gamma_1/b + \gamma_2/b$.

The two curvatures are related to the surface contour, $f(x)$, as

$$\kappa_1 = \frac{f''}{(1 + (f')^2)^{3/2}}$$

$$\kappa_2 = \frac{1}{x} \frac{f'}{(1 + (f')^2)^{1/2}}, \tag{2.9}$$

where the prime denotes differentiation with respect to x. Taken together, equation 2.2, equations 2.3 and the assumption of a uniform surface tension allows the governing differential equation for the fluid droplet shape to be written as,

$$\frac{d^2\tilde{z}}{d\tilde{x}^2} + \frac{1}{\tilde{x}}\left(\frac{d\tilde{z}}{d\tilde{x}}\right) + \frac{1}{\tilde{x}}\left(\frac{d\tilde{z}}{d\tilde{x}}\right)^3 = (2 + \beta\tilde{z})\left[1 + \left(\frac{d\tilde{z}}{d\tilde{x}}\right)^2\right]^{\frac{3}{2}}. \tag{2.10}$$

24

Here, $\tilde{x}$ and $\tilde{z}$ are x and z scaled by b for convenience. Notably, this equation has only one free parameter,

$$\beta = \frac{g\rho b^2}{\gamma}, \tag{2.11}$$

which makes it an ideal option for measurement – there is only one fit parameter in comparing a calculated shape to a measured drop shape. Equation 2.4 has no analytic solution and must be solved numerically. Luckily, the numerical solution was first calculated many years ago by Bashforth and Adams [28], who's names are generally associated with the equation.

2.5. Experimental Procedure

Below we outline the procedures of creating fluid emulsion droplets stabilized by a diblock copolymer and how confocal microscopy was used to image a full drop shape.

2.5.1. Materials and Solution Preparation

Polystyrene-block-poly(ethylene oxide) was used as received from Polymer Source (Canada). In this work polymer with 32 kg/mol and 11 kg/mol of PS and PEO blocks respectively was used. The polymer has a polydispersity index (PDI) of 1.06. As outlined in Table 2.1, two other molecular weights were also examined.

Table 2.1. Composition of block copolymer used.

Name	Polymer	PDI	Total Mn
DB1	PS32k-PEO11k	1.06	43.0 (Kg mol-1)
DB2	PS12k-PEO30k	1.10	42.0 (Kg mol-1)
DB3	PS90k-PEO45k	1.14	135.0 (Kg mol-1)

Organic compounds glycerin and toluene was purchased from Fisher Scientific. Organic solvents were dyed with Nile Red (9-Diethylamino-5H-benzo[a]phenoxazine-5-one) which was

purchased from MP Biomedicals, LLC. Nile Red is hydrophobic, and has low solubility in water making it ideal for imaging the organic phase of the emulsion. Highest grade mica was purchased from Ted Pella, Inc. Deionized water was produced with a Milli-Q purifier.

Solutions of 0.05% PS-PEO in toluene (by weight) were prepared and emulsified in a glycerin/water solution. The glycerin solution was 60% by weight glycerin. In order to broaden the droplet size distribution micropipette drop formation techniques were occasionally employed. Glass micropipettes were fabricated in the lab using a micropipette puller (Sutter Instrument Model P87) and borosilicate glass tubes (provided by Kimble & chase, 1.5-1.8 mm). An image of the instrument is shown in figure 2.5. The pull settings used in the experiment with arbitrary units are as follows: Heat – 920, Pull (force) – 250, Vel (pull velocity) – 244 and Time – 150.
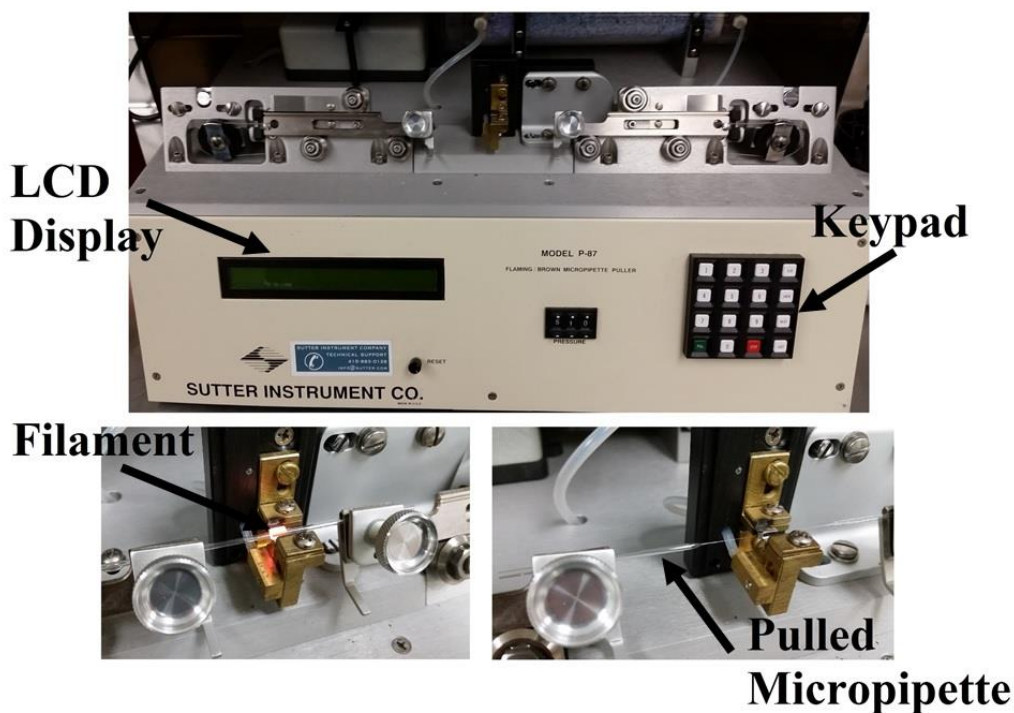
Figure 2.5. Micropipette puller set up with close up images of the filament in use and a pulled micropipette.

The diameter of the tapered glass pipette was determined by the point at which the tip was broken using a blade. The tips were often shattered or broken at an angle. To achieve an ideal 90

degree cut, the fire polishing technique was implemented. A kanthal A1 (iron-chromium-aluminum) wire (purchased from Sandvik) was heated using a DC voltage ($13 \pm 5\ V\ and\ 1.2 \pm 0.3\ A$) supply and the micropipettes were cut under an optical microscope.

Emulsion droplets were drawn from the solution with a pulled micropipette and placed in a glass cell filled with glycerine/water solution and capped with freshly cleaved, atomically flat mica. A schematic and an actual image of the curved mica and glass cell set up is shown in figure 2.6.
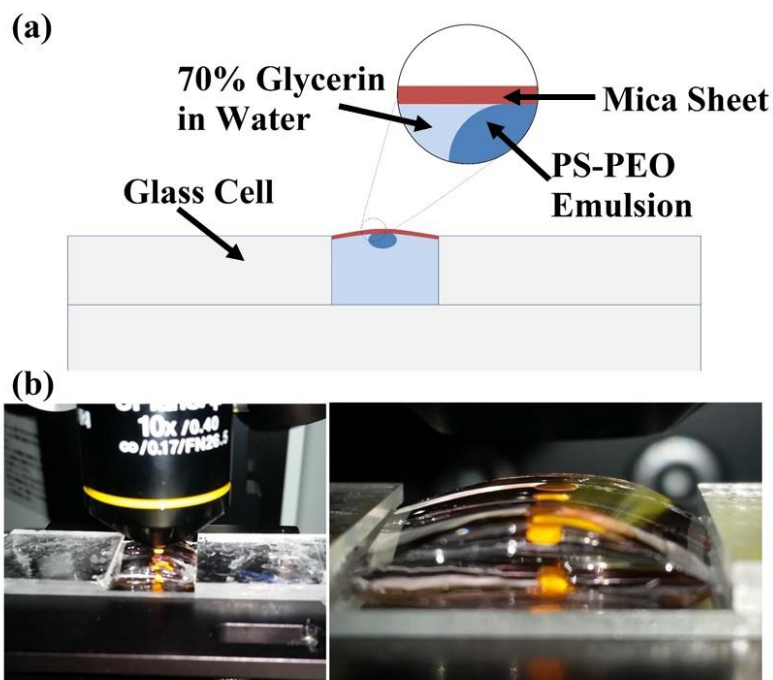
Figure 2.6. (a) Side view schematic representation of the glass cell and fluid emulsion droplet setup. (b) An actual image of the glass cell setup under the LSCM.

2.5.2. Laser Scanning Confocal Microscopy

The droplets were imaged using an Olympus Fluoview 1000 laser scanning confocal microscope (LSCM). An illustration of a typical laser scanning confocal microscopy setup is

shown in figure 2.7. The droplets were allowed to equilibrate for 3-5 minutes against the mica substrate before imaging.
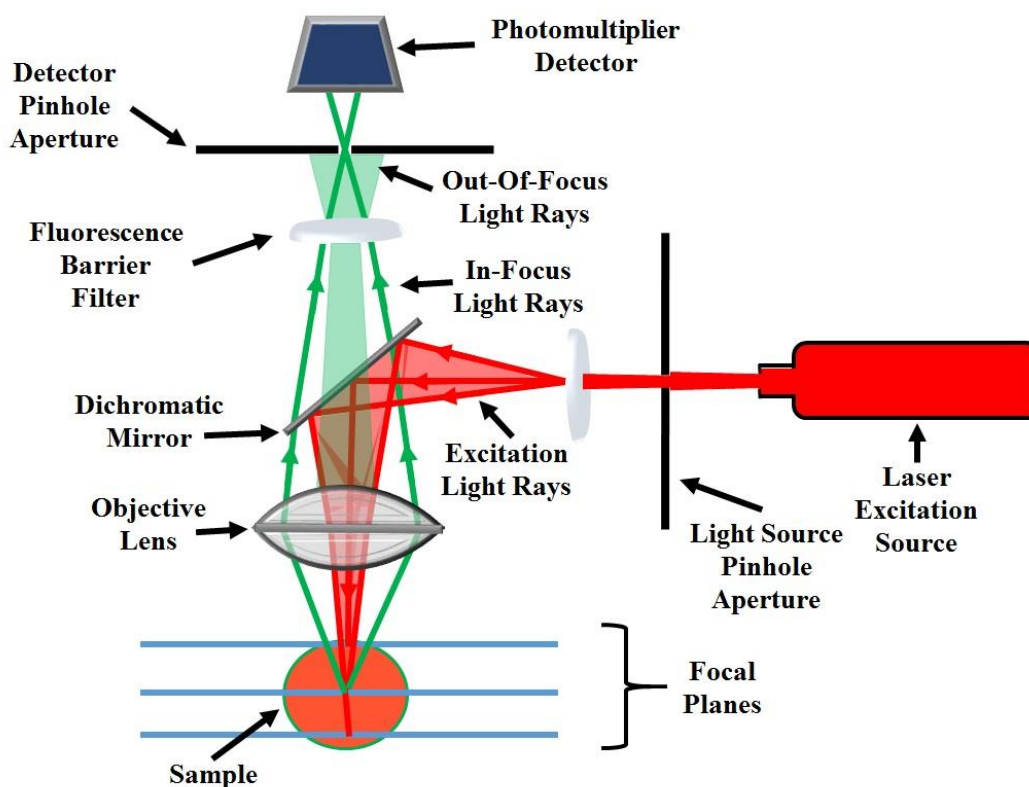
Figure 2.7. Schematic representation of the setup of a typical confocal microscope.

Several different wavelengths of laser were available in the LSCM system. However, 405 nm and 488 nm wavelengths were used to image the droplets. The Nyle red dye molecules were excited by either of the two wavelengths. Olympus microscope lenses of several different magnifications were used (5X, 10X, 50X and 100X).

3D images of droplet were captured using the LSCM. LSCM forms an ideal observation platform because it is capable of capturing, at high resolution, both relevant length scales necessary to model the deformation of a soft sphere. 1.) High resolution interference data (figure 2.8. and 2.9.) was used to calculate the shape near the contact region while 2.) the global shape of the dyed droplet was given by optically sectioning the drop (Fig. 2.8.).

28
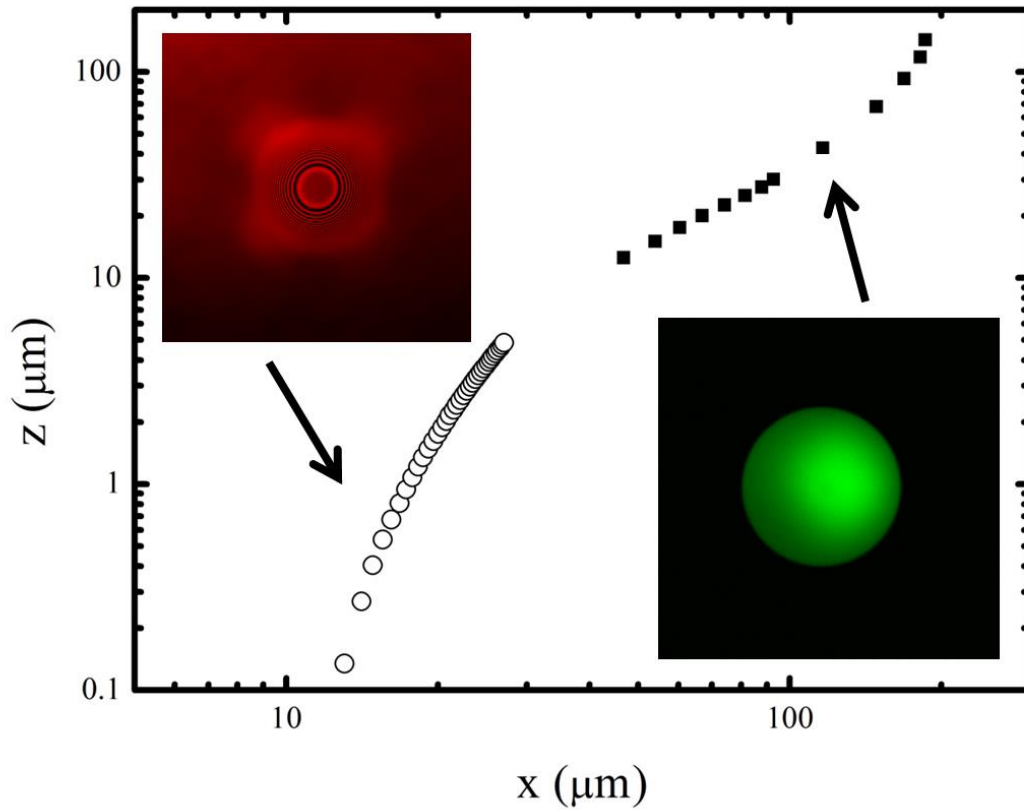
Figure 2.8. Experimentally measured drop shape of an individual PS-PEO coated toluene droplet combining data from both interference and optical sectioning. Note: Both axes are in logarithmic to show high resolution data over a large range.

The equilibrium position of the droplet surface was determined by calculating the distance between the mica surface and the droplet surface using:

$$h_j = \frac{j\lambda}{2n_w} \ (j \ = \ 0.5, 1, 1.5, 2.0\ldots), \tag{2.12}$$

where n_w is the index of refraction of the fluid in between the drop surface and mica (60% glycerine/water). It is assumed that the droplet surface bends monotonically away from the mica surface. The initial (from the left) low intensity part of figure 2.9 (b) belongs to zero order fringe and the first dark ring corresponds to $j = 0.5$. The resulting height profiles are presented in figure 2.8, along with the global shape of the droplet.

29
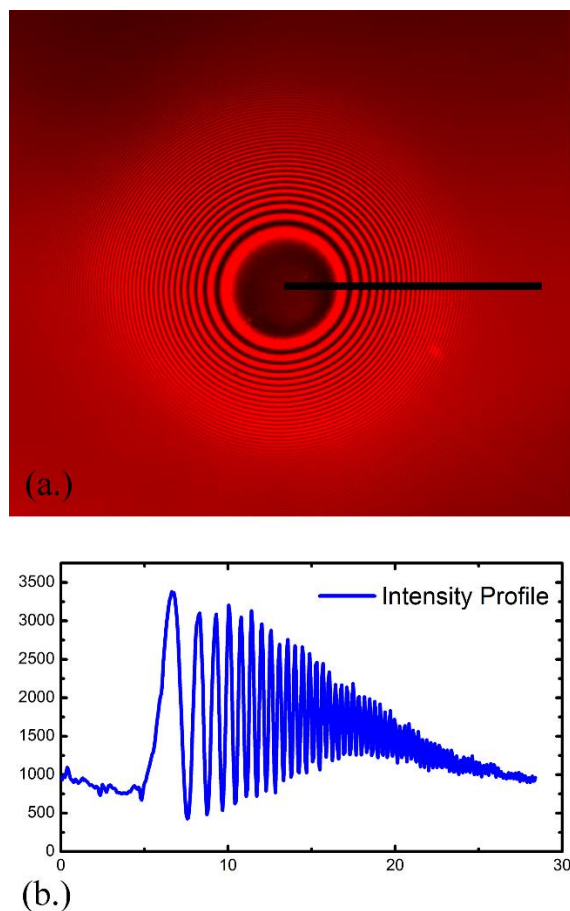
Figure 2.9. (a) LSCM image showing interference between light reflected from the mica surface and from the droplet surface. (b) Intensity profile through the center of the contact region.

2.6. Results and Discussion

Ensembles of PS-PEO armored emulsion droplets were successfully formed over a broad range of droplet diameters (10 μm – 1200 μm). These were imaged with LSCM and droplet shapes were calculated. The drops ranged from spherical to significantly distorted and all had non-zero contact patches of varying sizes.

As discussed above, there are two possible regimes of fluid drop deformation: 1.) if the droplet is small, the buoyant forces are very weak and the droplet takes on a perfectly spherical shape cut-off at the substrate contact or 2.) if the droplet size is large the drop will deviate from a spherical shape. Comparing the drop size with the capillary length, $\kappa^{-1} = \sqrt{\gamma/\rho g}$, gives a rough

estimate of the crossover between the two regimes. In our case, the difference in density between toluene and glycerin/water is 314 kg/m^3, and the surface tension will be of order 10 mN/m giving an estimated capillary length of about 6 mm [31-33]. The relatively large length scale suggests that most microscopic drops should be considered 'small', facilitating a relatively easy analysis by plotting the contact radius r against the drop radius R and fitting to equation 1.11. As can be seen in figure 2.10 the data cannot be fit by a single straight curve, verifying the quantitative weakness of the capillary length crossover estimate. The roughness of the capillary length estimate highlights the influence of the geometry of a high contact angle on the simple force balance argument from which the capillary number arises[5,34,35].

The smaller drop data shown in Figure 2.10 is well fit by equation 2.7, yielding a measurement of $\theta = 176 \pm 1$ degrees. The fit is easily verified by directly measuring the average contact angle of small droplets, here found to be $\theta_c = 175 \pm 1$ degrees. Ultimately, the measurement only allows us to calculate the ratio of interfacial tensions given by equation 1.11, which we find to be 0.997. Note that without further assumption or measurement we cannot uniquely define an interfacial tension for the oil/PS-PEO/water interface.

Above a drop size of about 100 um, the data clearly deviates from equation 2.7. Inspection of the drop shapes also shows a deviation from the perfect spherical shape, indicating clearly that the drops are being distorted by gravity. Figure 2.8 shows a typical large drop and several numerical solutions to the Bashforth-Adams equation which we solved using GNU Octave and MatLab. Each numerical drop represents a specific choice of β, and the data is fit by iteratively changing β. In this case the drop shown is well fit with $\beta = .05 \pm .03$, or an interfacial tension of $\gamma = 10 \pm 6$ mN/m.
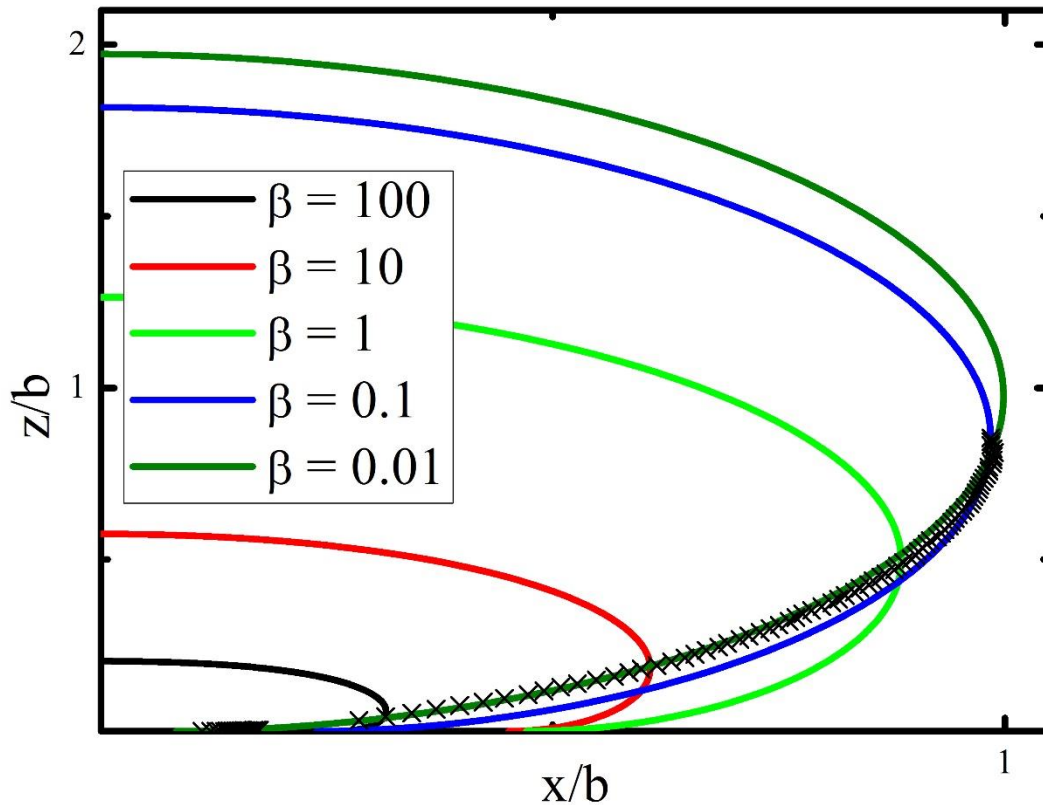
Figure 2.10. Droplet shapes for a range of β values, generated from the Bashforth and Adams model (solid lines), X symbols show an experimentally measured drop shape.

Fitting each drop individually is tedious, and only possible with a high resolution 3D image of a droplet, which is only available with LSCM. However, each curve generated by a specific β has a unique value of r/b and R/b. Inverting β to isolate b and using a system specific value for density allows the construction of a family r(R) curves which differ only in surface tension (see figure 2.9). The family of numerical curves can then be fit to the ensemble of experimentally measured r and R values and a statistically accurate measurement of the interfacial tension can be made. Figure 2.10 shows the result for the 0.5% PS-PEO/toluene in 60% glycerine/water emulsion which is found to have an interfacial tension of $\gamma = 9 \pm 1$ mN/m.
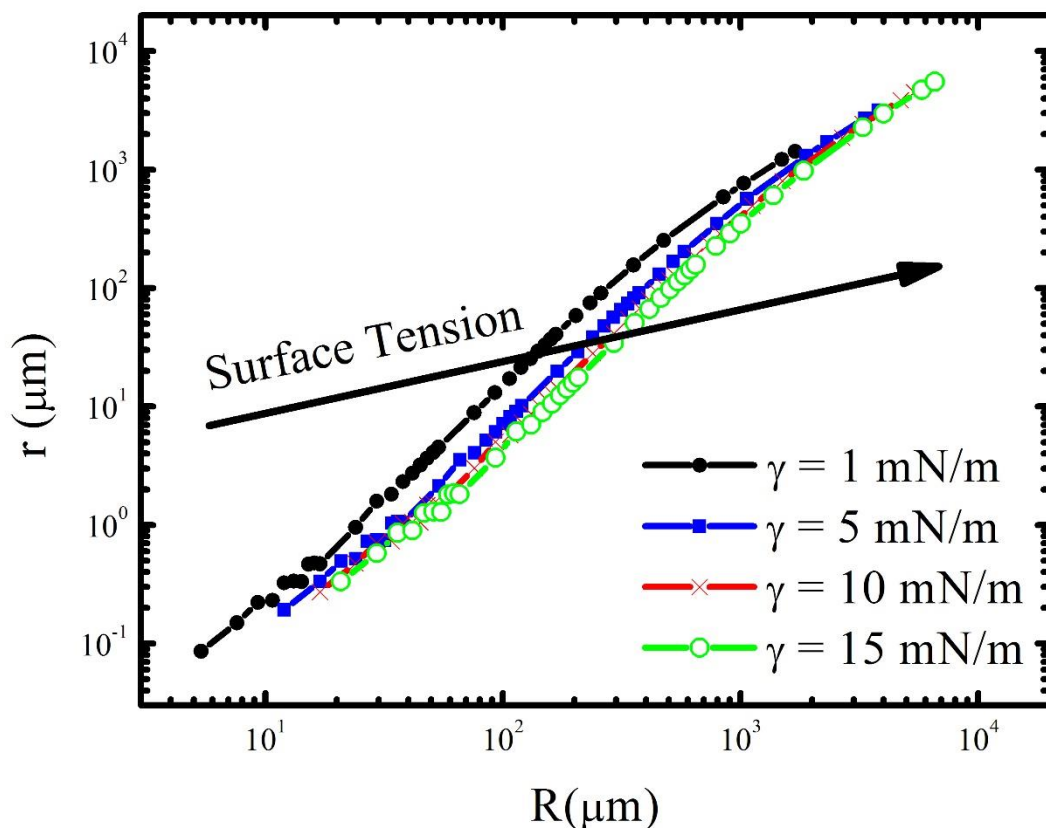
Figure 2.11. Theoretical r vs. R curves for varying surface tensions, for droplets with a change in density of inner fluid and outer fluid (toluene to 60% glycerin in water) of 314 kg/m3. The arrow across the plot indicates the shift in curve as the surface tension increases.

Figure 2.11 shows r(R) curves for three different PS-PEO molecules at identical concentrations of toluene and glycerine/water solution. The second molecule (DB2) was chosen to be the inverse of the first molecule having a long PS block and short PEO block. The second molecule should occupy approximately the same amount interfacial area as does the first molecule (as the total length is similar), so we would not expect to see a significant change in interfacial tension. The third molecule (DB3) was chosen to be similar in block length ratio, but with a larger total molecular weight than the first molecule. In this case, each molecule will occupy more of the interface due to the increased size and we would expect to see an increased interfacial energy due to the decreased coverage.

33
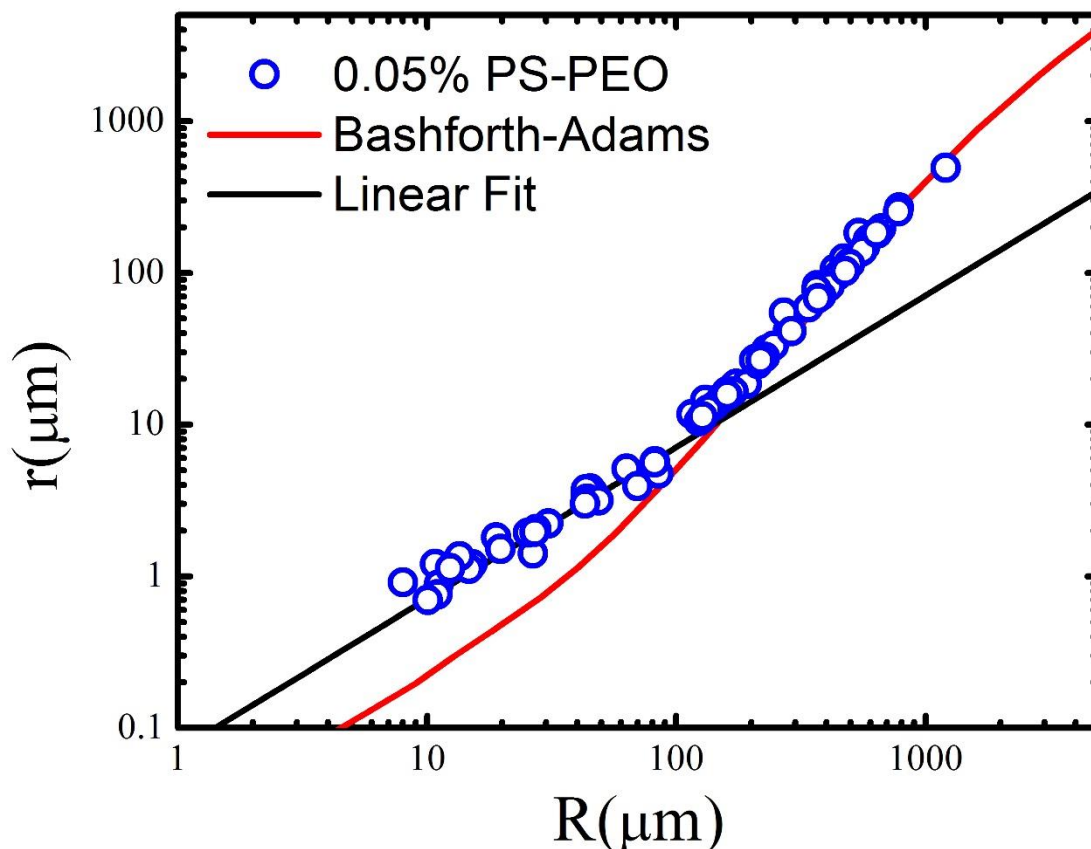
Figure 2.12. Experimental data, for Rmax less than 100 μm, fitted with capillary model and the rest with Bashforth-Adams model (with a surface tension of 10 +1 mN/m). The slope of the fitted line of the capillary model corresponds to $r = R \sin\theta$, $\theta = 176^0 \pm 1$.

Figure 2.12 and 2.13 show the outcome of the experiment. All drops are well fit by the Bashforth-Adams model, and interfacial tensions can be measured. The inverted molecule (DB2) was found to have $\gamma = 12 \pm 1$ mN/m, very close to the original molecule. The larger block copolymer (DB3) was found to have $\gamma = 35 \pm 2$ mN/m. The interfacial tension of the larger molecule is much larger than the original molecule and, in fact, very close to the interfacial cost of a bare water/toluene interface (as measured by pendent drop). Even so, the emulsion remains stable verifying the presence of an interfacial layer (pure toluene very quickly wets the mica surface). Finally, our measurements are consistent with our own pendent drop and micropipette measurements, as well as with the existing literature for PS-PEO measurements [36,37].
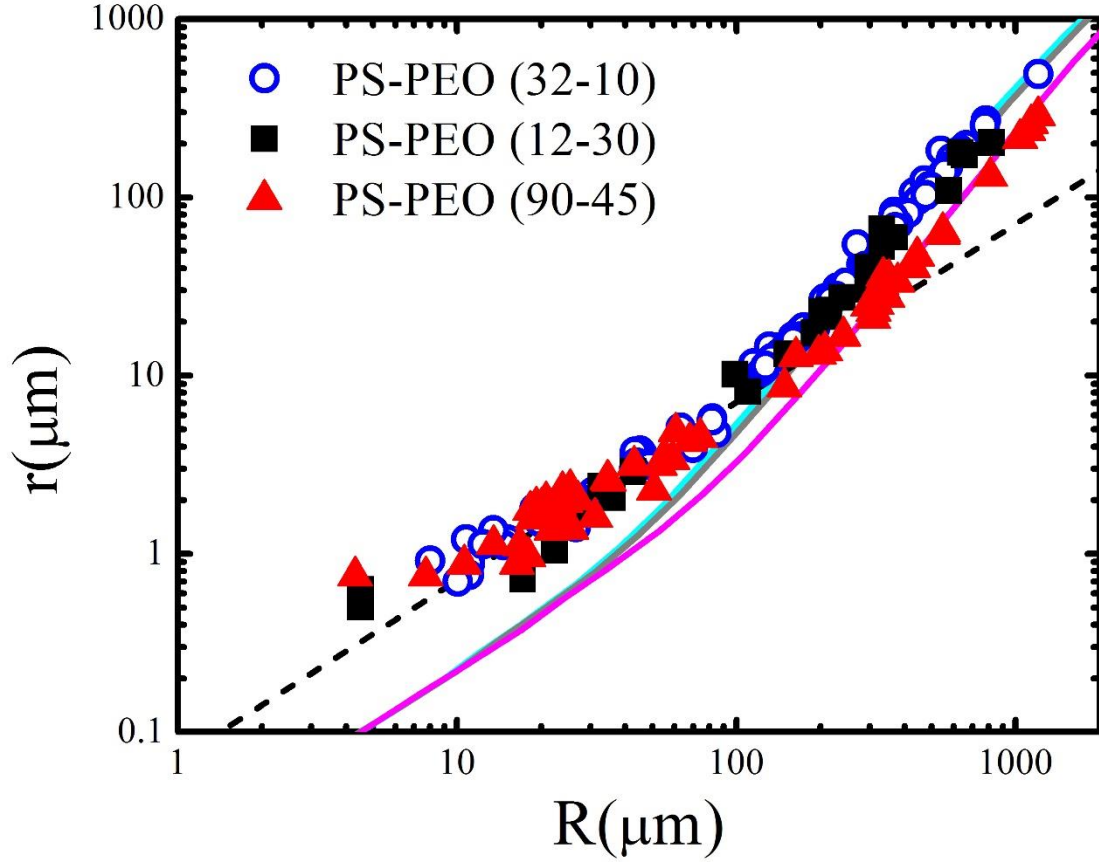
Figure 2.13. Experimental data for different molecular weights of PS-PEO fitted with Bashforth-Adams model.

All three ensembles approach the same curve in the small drop region, suggesting a fixed contact angle for all drops. Without a direct interfacial tension measurement this observation might lead to the naive presumption that all three drops have identical interfacial properties. The reality, however, is that a contact angle only measures a ratio, and both γ and $\gamma_{sv} - \gamma_{sl}$ can change proportionally to one another. In this case γ_{sv} is identical in all cases, hence γ_{sl} is also different for each molecule.

2.7. Summary

In this chapter we have developed the traditional sessile drop technique into convenient method to measure surface properties of fluid droplets. Our analysis of the fluid droplets has

focused on the classical Bashforth-Adams equation and the Young-Dupré equation. Combining this creates a 'one pot' measurement of all three relevant interfacial energies (although only γ and a difference between γ_{sv} and γ_{sl} can be precisely established). The measurement uniquely ranges from microscopic to macroscopic, a considerable advantage compared to standard techniques.

The simple experiment allows us to measure the surface tension of an ensemble of droplets with better accuracy than modeling a fit for each independent droplet. Furthermore, these experiments only involve a drop size and a contact patch size which can be achieved using a simple optical microscope. We have also shown that this technique is sensitive to small changes in surface tension. The surface tension of oil droplets stabilized by different length PS-PEO molecules were successfully measured.

3. SYNTHESIS AND MECHANICS OF ELASTOMERIC SHELLS FILLED WITH AN INCOMPRESSIBLE FLUID

3.1. Introduction

Similar to chapter two, our primary goal is to advance the understanding of encapsulation and targeted drug delivery systems. In this chapter, we present a novel technique to synthesize elastic shells and characterize their mechanical response, effectively measuring the Young's modulus. Physical properties of thin, nanoscale shells are typically difficult to measure. We utilize a sessile drop geometry and develop the relevant theory needed to analyze an elastic shell.

Lipid and block copolymer vesicles, for example, are now commonplace in the pharmaceutical industry largely because they allow a drug to have significantly increased circulation time [38]. The technology, however, often remains far from achieving the fast responsiveness to external stimuli that is desirable in modern materials and targeted delivery schemes. An obvious path forward involves harnessing mechanical instability in the structure, as mechanical instability represents one of the fastest types of response available in nature [39]. In the fluid state elastic instability is unlikely, hence there is little that can be done to increase delivery speed. Changing the capsule from liquid to solid, however, would greatly increase design options. Capsules which are currently in use have properties which have already been optimized for achieving the drug delivery goals. What is needed, are materials and structures which mimic existing capsule properties and yet open the door for the possibility of engineered instabilities.

Changing from liquid to solid, with the goal of maintaining similar large scale properties and non-interacting surface properties, presents challenges not only to material design, but also to measurement. A fluid-like drop can be measured in a pendent drop experiment but an elastic capsule cannot. Motivated by the fluid droplet measurement technique presented in the previous

chapter, the sessile drop technique was used to measure the mechanical properties of an elastic interface.

Our technique has advantages over other measurements such as pendant drop [24-27] and micropipette aspiration methods [22,29]. The micropipette aspiration method relies on pulling a droplet into a narrow pipette, and comparing the applied pressure to the deformation [22,29]. The sharp bending at the pipette opening often leads to rupture in an elastic shell [12]. The sessile drop measurement rarely leads to such high or localized stresses as the droplet is 'pressed' into a flat substrate by a buoyant force. The pendent drop method is another reliable technique that can be used to measure similar material properties. The pendant drop method works well for many fluid interfaces but in order to adapt the measurement to an elastic interface, the surface has to be fabricated after the fluid drop is formed [24-27]. For shells synthesized after creating a fluid drop, there is there is no limit on the polymer concentration as it is always attached to a reservoir of polymers. Therefore, sessile drop geometry provides a better technique to measure already created shells.

Elastic shells were synthesized using a novel method to match the deformation characteristics of the fluid droplet. Specifically, we use polystyrene-b-poly (acrylic acid)-b-polystyrene (PS-PAA-PS) to synthesize elastic shells. We note that our treatment considers the low adhesion limit, opposite to much existing analysis [40-42]. The elastic shells are well described by both a simple scaling model, and a more detailed mechanical model similar in structure to the Bashforth-Adams fluid model (described in chapter 2).

3.2. Theory of Elastic Shells

3.2.1. Scaling Theory of Shells

The deformation of a thin elastic shell by a flat surface is a fascinating classical problem which is still of considerable modern interest [30,39,41,43-47]. Interest in the problem stems not only from its connection to many industrial applications, but from the complexity of the deformation itself. During deformation, a force, F, is applied to a spherical shell pushing it a distance, e, into a smooth flat surface. As the force is increased from zero, the shell undergoes 3 different behaviors: 1.) initially the shell is flattened only locally on its surface (the interior surface of the shell remains spherical when $e < h$), 2.) the shell becomes flattened over some larger region $(r \sim h)$ and 3.) the shell buckles inward focusing bending into a ring (Pogorelov ridge [48-50]) of radius r $(r > h)$. In this work we limit our discussion to stage 2 deformations as stage 1 occurs on nanoscopic scales in our system, and stage 3 is never observed. Additionally, we emphasize that we neglect any adhesion energy between the shell and the indenting surface [40-42].
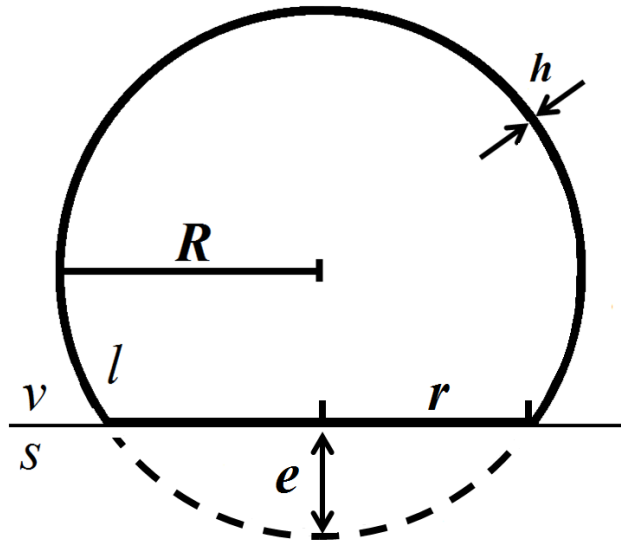
Figure 3.1. Side view schematic of a spherical elastic shell of thickness h with a linear deformation of e.

Figure 3.1 shows the basic geometry of the deformation in stage 2, where the shell takes on the shape of a spherical cap. The elastic energy stored in the shell is a sum of the energy required to bend the segment of arc flat ($\sim B/R^2$, where B is the bending modulus of the shell) and the energy stored in compressing the arc length such that it fits into the smaller flattened region ($\sim K\varepsilon^2$ where K is a stretching modulus). To first order, the change in length of the arc in going from flat to curved is given by r^3/R^2 [39]. Normalizing change in arc length by the contact patch size r gives the scale of the strain ($\varepsilon \sim r^2/R^2$). With Young's modulus, E, and shell thickness h the energy per unit area can be written as [39]:

$$\frac{U}{R^2} \sim \frac{Eh^3}{R^2} + Eh\left(\frac{r^2}{R^2}\right)^2 \tag{3.1}$$

Comparing the stretching and bending terms in equation 3.1 yields the conclusion that $r \sim \sqrt{hR}$ in this deformation regime.

In the present work, two additional details must be included in order to arrive at an accurate scaling argument. First, contrary to the classical calculation which results in equation 3.1, in the sessile drop geometry the work done in compressing the sphere is proportional to the sphere size through the gravitational potential acting over the indentation distance ($Fe \sim \rho g R^3 e$). Secondly, the calculation leading to equation 3.1 assumes the shell to be filled with an infinitely compressible liquid which allows the strain to be confined to the contact region. In our experiments the sphere is filled with an incompressible liquid, thus the strain energy is spread evenly over the entire surface of the shell ($\varepsilon \sim r^3/R^3$). Guided again by our experimental system in which $h \ll e$ we make the assumption that the bending term is negligible and by equating the work done to the elastic energy, we write a new scaling relation:

$$r \sim \alpha R^{3/2} \tag{3.2}$$

The constant takes on a similar form to β in Bashforth-Adams equation, $\alpha^4 \sim \rho g/Eh$. This prediction is notably different from other estimates (largely due to the choice of strain energy) but is justified by its fit to the experiment as discussed below [51].

To put equation 3.2 in proper context it is useful to compare with the scale of deformation in other spherical, elastic geometries. Consider a shell filled with a compressible fluid as discussed initially. Equation 3.1 and the assumption of a dominant stretching energy lead to the relation $r \sim \alpha^{1/2} R^2$. This is an interesting limit, however, it is important to point out that it is only applicable over the tiny range ($h < r < \sqrt{hR}$) [39]. On the other hand, the indentation force between a solid elastic sphere and a flat rigid wall has been known to scale as $F \sim Er^3/R$ since the time of Hertz [52]. With a buoyant driving force that is proportional to the sphere volume, the contact radius is found to scale as $r \sim (\rho g/E)^{1/3} R^{4/3}$. Equation 3.2 lies between the two limits as one might expect.

3.2.2. Mechanics of Shells

A more complete formalism for an elastic shell in contact with a plate while under the influence of gravity can be found following the arguments detailed in chapter 2 above for a large fluid drop. There is a tension that resists elongation of the surface; however, the tension now has two components – a pre or initial tension, τ_0 and an elastic tension due to stretching of the shell. Most generally, the tension will depend on position, $f(x)$, as the elastic shell can bear shear forces. Thus a constitutive equation is also necessary. Here we will employ a Neo-Hookean model due to its generality:

$$U = \frac{Eh_0}{6}\left(\lambda_1^2 + \lambda_2^2 + \frac{1}{\lambda_1^2 \lambda_2^2}\right) \tag{3.3}$$

where U is strain energy per area, h_0 is the shell thickness and $\lambda_{1,2}$ are the principal stretch ratios (the third principal axis is absorbed by the incompressibility condition $\lambda_1\lambda_2\lambda_3 = 1$). In general, the stretch ratios depend on position within the shell, requiring detailed knowledge of the history of the deformation to be recorded [24]. For simplicity, which is justified by the relatively small deformations in our experiment and the incompressible interior fluid, we make the assumption that the strain energy is evenly distributed over the shell, hence $\lambda_1 = \lambda_2 = (A/A_0)^{1/2}$, where A is the final surface area and A_0 is the initial area. Together with equation 3.3 and the theory of elasticity, the tension is:

$$\tau_1 = \tau_2 = \gamma_0 + \frac{Eh_0}{3}(1 - \lambda^{-6}). \tag{3.4}$$

Equation 3.4 replaces γ in equation 2.11, and the differential equation (equation 2.10) can be solved to yield a shell shape. We point out that qualitatively there is little difference with the fluid model; a given tension relates to a given value for β and a particular drop shape. The main difference in including elasticity is that now drops of differing size will have differing tension.

3.3. Experimental Procedure

In addition to the organic solvents mentioned in chapter 2, tetrahydrofuran (THF) was bought from Fisher Scientific. Polystyrene-b-poly (acrylic acid)-b-polystyrene (PS1k-PAA50k-PS1k) with a PDI of 1.08 was purchased by Polymer Source (Canada).
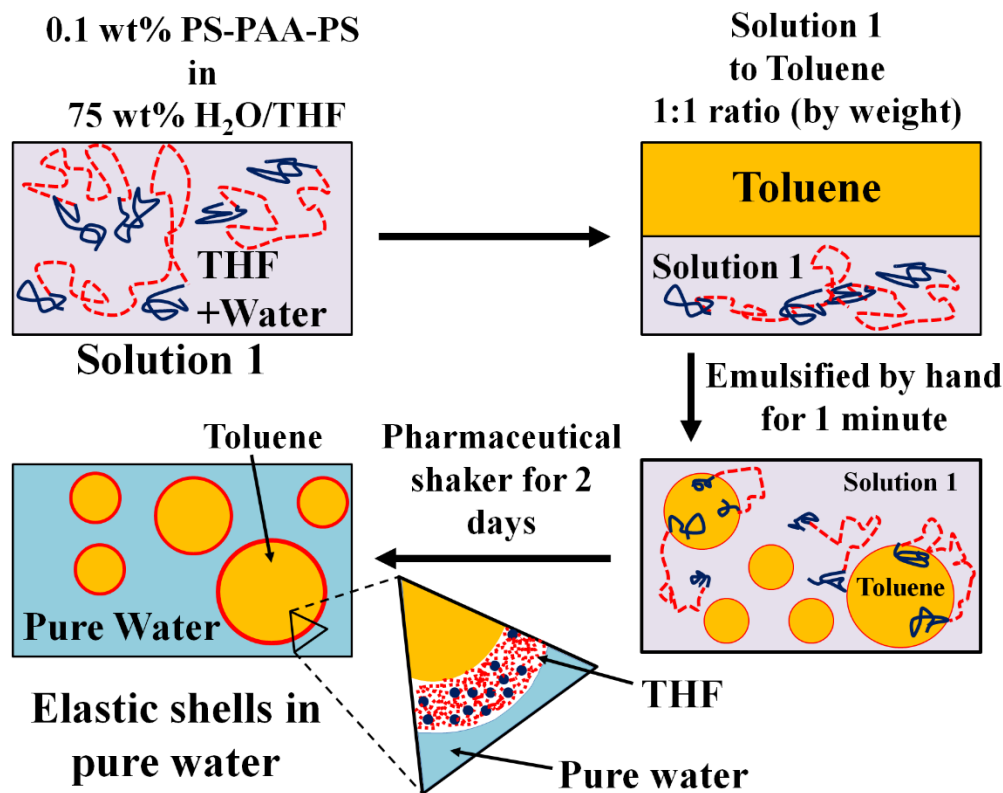
Figure 3.2. A schematic showing the process of PS-PAA-PS elastic shell fabrication. The basic mechanism is interfacial self-assembly coupled with a change in solvent quality.

Elastic shells were created through a process of guided interfacial self-assembly and gelation of the PS-PAA-PS molecules inspired by recent work with similar copolymers [53,54]. First, 0.1% of PS-PAA-PS was dissolved in water/THF (75% water in THF) by weight (solution 1). This mixture of solvents was necessary to adequately dissolve the triblock. Next, solution 1 was added to toluene in a 1:1 ratio (by weight). This mixture was then emulsified by hand-shaking for one minute and was set on a pharmaceutical shaker for two days. During this stage several processes take place. First toluene drops form within the solution 1 phase. The oil/water interface allows self-assembly of the triblock copolymer to occur (similar to PS-PEO (in chapter 2), PS-PAA-PS is amphiphilic and readily adsorbs to water/oil interfaces). Finally, the larger reservoir causes the THF concentration in solution 1 to plummet, and thus the solubility of the polymer also

drops. The long time on the shaker allows the solvents to reach this new 'equilibrium' (the mixture as a whole is in a non-equilibrium state as the drops do not coarsen). The emulsion drops were then transferred to a 20 ml glass vial filled with pure water. This allows any remaining THF to leave the drops for the much larger water reservoir. After hours to days in pure water the drops were then inserted into a glass cell filled with 60% glycerine/water mixture and capped with a freshly cleaved mica sheet. Samples were then imaged using LSCM as described above.
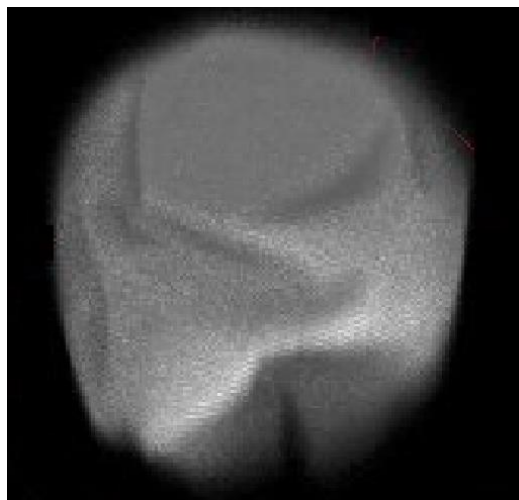
Figure 3.3. LSCM 3D image of a crushed elastomeric shell confirming that the shell fractures and crumples analogously to a crumpled up paper ball. Note the shell is still (mostly) encapsulating a toluene droplet which continues to push the shell upwards against a mica sheet (not visible).

The presence of an elastic shell could be confirmed in several ways. First, droplets were transferred to clean electronics grade silicon substrates and allowed to dry. The dried structures resembled crumpled elastic sheets. More directly, droplets could be mechanically crushed with a micropipette and subsequently imaged. Figure 3.3 shows a typical post crushing image in which a structure surrounding a toluene drop shows sharp cracks, ridges and d-cones typical of a crumpled elastic material. Prior to crushing, the shell is a smooth continuous structure.

The 'crushed' shells did not change over the course of the experiment (several hours) verifying the existence of a rigid, non-fluid structure. The average thickness of the dried shells on

silicon wafers was scanned using an atomic force microscope (AFM, Veeco Dimension 3100) to be 10 ± 2 nm. To mimic swollen properties of the shells, AFM nano-indentation was performed on wet, PS-PAA-PS which was drop cast on a silicon substrate. Completely submerged shells were too difficult to hold in fixed position due to their extremely low adhesion energies. We measured a Young's modulus of $0.12 \pm .02$ MPa, but do not believe it to be directly comparable to the modulus of the shells. In our experiments the PS-PAA-PS shell is created under non-equilibrium conditions (gel modulus is very sensitive to the method of creation) and resides at a toluene/water interface and is likely swollen by both solvents (not just water).

3.4. Results and Discussion

For simplicity, we focus on the largest block copolymer molecules and synthesize an elastic shell encapsulated droplet with a matching mechanical response. The shells are made using a PS-PAA-PS triblock layer which forms a physical gel on the droplet surface. Our technique is outlined in the previous section. Polyacrylic acid was chosen as a majority phase because of its similarity to PEO and because its polyelectrolyte nature makes it sensitive to changes in local ion concentration, facilitating future material responsiveness (see appendix A).

There are very few methods available for characterizing droplets created in this way. AFM based indentation methods are complex, especially as the high PAA content makes the shell material very slippery and non-interacting – similarly to the PEO brushes in the diblock case explored above. Pendent drop methods require very large drops [24-27], and micropipette-based methods often lead to fracture of the thin shell [39]. The sessile drop method is ideal for characterizing the drops exactly as they are formed; it does not require large stresses (avoiding fracture) and it is impartial to the low adhesion of the droplets.
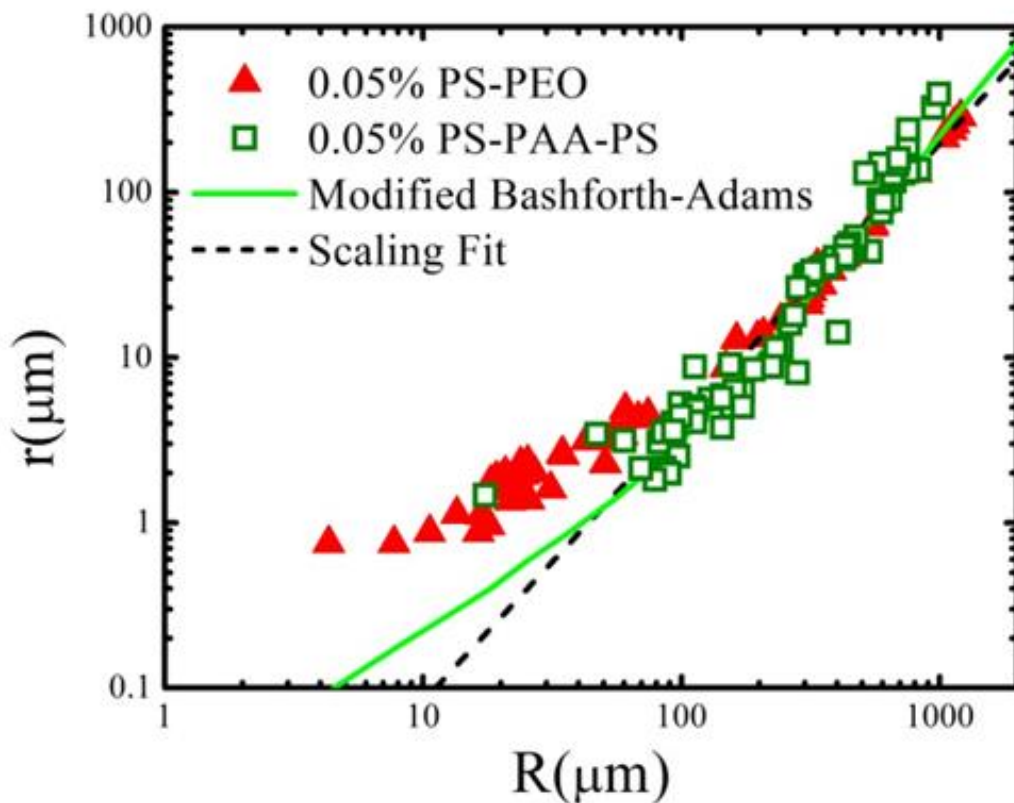
Figure 3.4. PS-PEO data from figure 2.11 with similarly measured PS-PAA-PS shells. Solid line is a fit to the mechanical Bashforth-Adams equation, yielding a tension of 35 ± 5 mN/m and $Eh_0 = 4 \pm 4$ N/m. The dashed line is the scaling fit described in the text.

Figure 3.4 shows the large molecule PS-PEO data (from chapter 2) along with r(R) data collected for an ensemble of elastic shell encapsulated toluene droplets. Qualitatively, the two sets of data are very similar and therefore satisfy our primary goal. The slight upturn at largest droplet sizes may indicate the presence of thermal undulations (slack) in the thin shells, however, the upturn is comparable to the noise in the measurement. The noise stems from the roughness of the membrane thickness (RMS = 1.8 nm) and its influence on the contact patch. Similar to shell thickness measurements, the surface roughness was measured using AFM images of dried shells.

In order to compare with the scaling discussed in section 3.2.1, the shell ensemble is fit with $r = mR^n$ (the dashed line in fig 3.4) yields an exponent of $n = 1.7 \pm 0.2$ and a proportionality

constant of m $= 1.7 \times 10^{-3}$ µm$^{-(n-1)}$, in close agreement with the predicted scaling argument (equation 3.2). Constraining n to 1.5 leads to a tension of ~0.18 N/m (assuming equation 3.2 is an equality). Using the measured shell thickness, the Young's modulus of the shell can be estimated, $E = 1.8 \times 10^7$ Pa. While measurements are within the range expected for a swollen PS-PAA-PS gel, the scaling argument has several weaknesses. First, like any scaling argument equation 3.2 should not be considered quantitatively accurate. Second, the scaling doesn't consider the possibility of residual strain in the membrane and does not explicitly include any contribution from the two fluids present. The scaling can only identify the magnitude of an elastic tension in the absence of any other pre-tensioning mechanisms. Therefore, the scaling argument will necessarily lead to an overestimate of the modulus. For example, an interfacial tension of 35 mN/m could be interpreted as a 10 nm thick membrane with a Young's modulus of 10^6 Pa, or as a bare toluene/water interface with no additional (elastic or other) tensions. Furthermore, in this specific case the fit is error prone as the data only ranges over 1 order of magnitude in drop sizes. The importance of the scaling is simply that the data shows agreement with the basic underlying physics; there is a tension in the interface, and the incompressible interior fluid distributes any local deformation over the entire sphere. Quantitative detail must come from a more advanced treatment of the sphere.
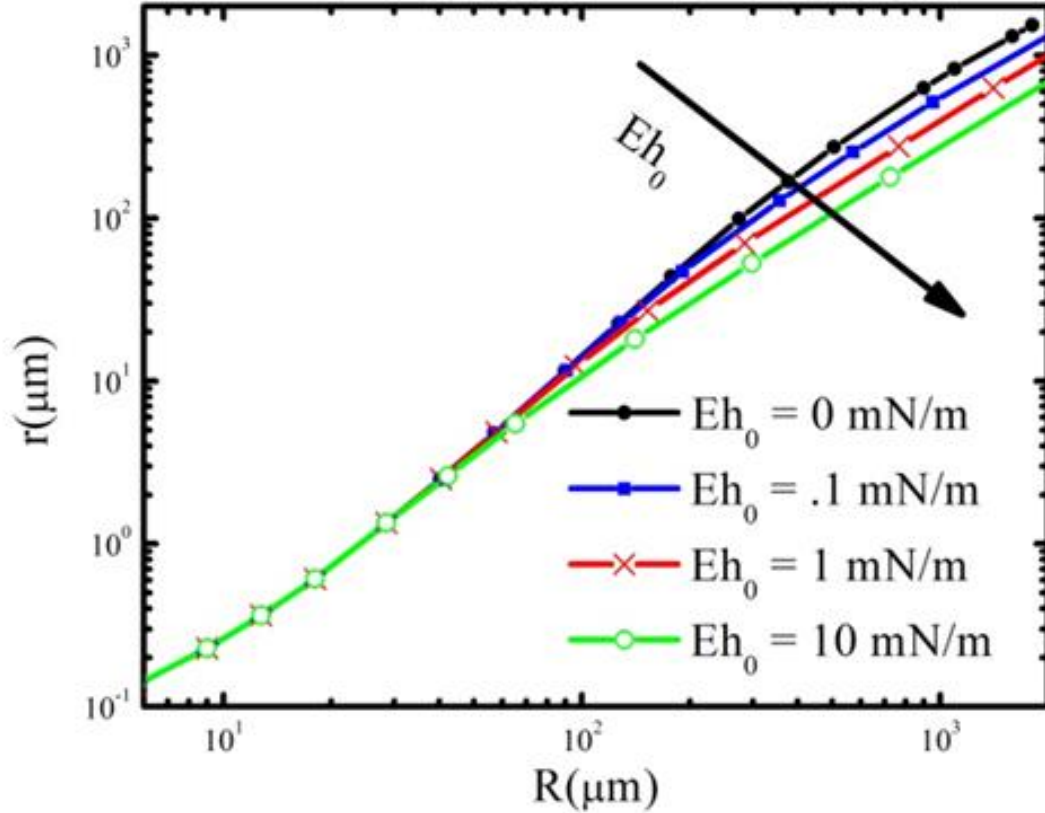
Figure 3.5. Sample r(R) curves generated with the mechanical model. Each curve has a fixed tension of $\tau_0 = 1$ mN/m. Eh_0 is as shown in the caption.

To increase our accuracy, we opt for the more complete model as outlined in section 3.2.2 above. Contrary to the pendent drop experiments, the governing differential equation cannot be directly solved here [24-27]. Instead, drop shapes are generated for various values of β (as was done for the fluid droplets in chapter 2). The numerically generated droplet shapes allow the volume and surface area of each drop to be accurately calculated. Assuming the volume is fixed and the drop was formed in a spherical shape, an initial surface area can be calculated and used to find the total areal strain on each drop. The strain can then be used to calculate the elastic tension in the shell (equation 3.5) for a given initial tension and elastic modulus. r/b and R/b values can again be converted to an r(R) curve as was done with the fluid droplets. The data shown in figure 3.4 is well fit with $\tau_0 = 35 \pm 5$ mN/m and $Eh_0 = 4 \pm 4$ N/m. In this experiment, even the largest

48

drops in the ensemble strains only reach 3% and the experiment is dominated by the intrinsic tension (production of larger droplets were prohibited by fracture during droplet transfer). The scale of the tension demonstrates that the interface is still largely dominated by toluene/water contact and is indeed insensitive to the actual modulus of the shell. That the tension can be decomposed into an intrinsic and an elastic component is an important outcome of the measurement; without accounting for both sources of resistance to deformation, real material properties will not be properly measured.

The measurement also explains how the two droplets, one fluid and one elastic, can have the same response to a deformation. Both are dominated by a strain independent interfacial tension. This also sets the stage for further development of elastic spheres as replacements for existing fluid like systems. To 'copy' the properties of a fluid drop, the elastic shell must be thin enough or have a low modulus such that the condition $\tau_0 \gg Eh$ is met. In this case, one need only control the bare interfacial tension.
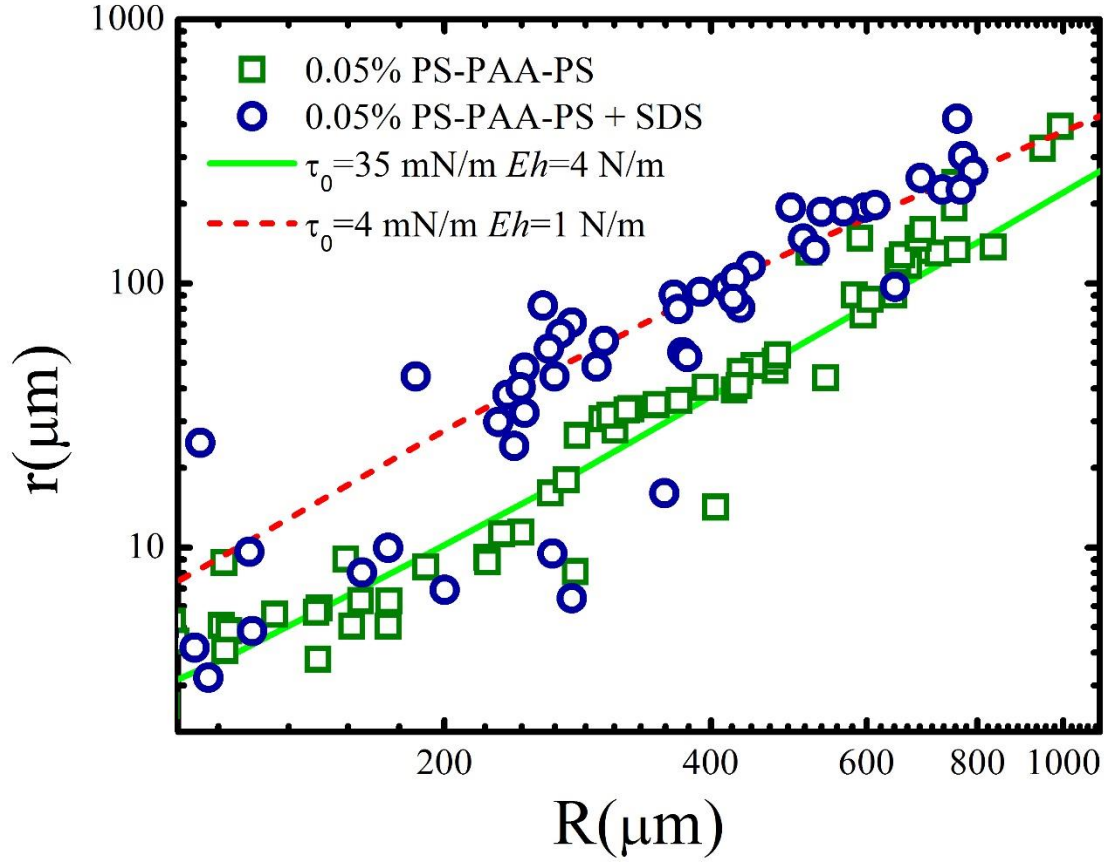
Figure 3.6. PS-PAA-PS elastic shell coated droplets in glycerine/water (open squares) and in glycerine/water with SDS (open circles). Fits to the modified Bashforth-Adams model are shown for both sets of data.

The large error in determining the mechanical contribution to the tension is somewhat unsatisfying. The measurement can easily be improved by decreasing the toluene/water interfacial tension. To do so, the measurement of a separate ensemble of droplets was completed after the droplets were injected into a sample cell saturated with the small molecule surfactant sodium dodecyl sulphate (SDS). The surfactant reduces the fluid-fluid interfacial tension, thus increasing the importance of the mechanical tension. Figure 3.6 shows the result. The ensemble is will fit with $\tau_0 = 4 \pm 1$ mN/m and $Eh_0 = 1 \pm 1$ N/m. Taken with the surfactant-free initial measurement, the overall confidence in the tension measurement is greatly increased. This final

measurement also shows how the surfactant can be a valuable tool in adjusting the exact mechanical properties of a drop to match the properties of other fluid drops.

3.5. Summary

We have synthesized a fluid enclosed elastic shell having similar mechanical properties to a fluid-filled block copolymer-stabilized emulsion drop. Successful mimicry of the mechanical properties of fluid-like capsules with an elastic system opens the door to the development of elastic instabilities in existing delivery schemes. Additionally, we have developed the sessile droplet into a convenient, simple and universal tool to measure the static properties of any microscopic soft sphere. The contrast between these two systems, elastic and fluid, demonstrates the universality of the technique.

We used a novel method to create an elastic shell on an oil interface and modelled the shells in two different ways. First, a simple scaling estimate was constructed and secondly a full elastic version of the Bashforth-Adams equation was considered. Due to the small strains in play, the elastic model was simplified resulting in a mathematical structure very similar to ordinary Bashforth-Adams fluid droplet model. Both methods provide quantitative estimates of the material properties of the elastic shell, although we note that our current system is dominated by an intrinsic interfacial energy rather than the elastic modulus of the shell. While the dominant tension is accurately measured, we can only set an upper limit on the value for the elastic modulus of the PS-PAA-PS shell.

On the fundamental side, the PS-PAA-PS spheres demonstrate an often ignored limit for soft spheres – a low adhesion soft mechanical shell with a fixed volume constraint. In this limit, little is known about the elasto-capillary forces including how and when instabilities may occur.

A new experimental system, such as the PS-PAA-PS shells synthesized here will create new opportunities to expand our understanding and use of material systems in this limit.

4. INFLUENCE OF BLOCK COPOLYMER ON THIN FILM DRAINAGE

4.1. Introduction

In this chapter, we move away from the static properties of block copolymer interfaces and study the dynamics of a fluid flow through a polymer brush. The work is motivated by targeted drug delivery systems. Typically, advance drug delivery systems hide the drug inside a spherical capsule, transport it to the required destination, the capsule interacts with the walls of the infected site and the drug is released [8,10,38,55]. It is important to understand the fundamental physics of the interactions between the capsules and cell walls to further advance the drug delivery technology. As a first step towards fully understanding these interaction, we study an idealized version of a polymersome which is an oil droplet with a polymer brush at the interface approach a flat wall (mica).

As a droplet or a bubble approaches a solid substrate in a homogeneous fluid, several dynamical processes can occur. Owing to their stiffness (or deformability) of the surface, the droplet can either 1) flatten or 2) buckle as it reaches the wall. Flattening of the drop as it reaches the wall was observed in the elastic shells discussed in the previous chapter. As oppose to a fluid droplet, the elastic droplets have a surface which can bear a shear force. This results in stretching the membrane instead of buckling. In the case of a fluid droplet, the contact region buckles in as it approaches the wall. This buckling of the droplet surface results in trapping a thin film of the continuous phase. The thin film drains out until a critical film thickness is reached and the droplet or the bubble ruptures or the fluid droplet reaches an equilibrium state [56-60]. Droplets and bubbles approaching walls or approaching other bubbles has been studied extensively [56-64]. The dynamics of droplets and bubbles covered with small surfactant molecules have also been studied [63-66]. Thin film drainage involving small surfactant covered interfaces are typically driven by

forces such as the disjoining pressure and hydrodynamic forces. In this study we change the complexity of the problem by adding a long diblock copolymer molecule to the interface of the fluid droplet. Due to the large size of the chains we use, we assume that the surface is completely covered with polymer chains. In this study, the concentration of polymer at the surface remains constant due to low entropy compared with a small surfactant system. Therefore, we assume that there is no interfacial tension gradient in our system. While this eliminates disjoining pressure and electrostatic forces, (which are commonly discussed in thin film drainage processes) it also give rise to more complex boundary conditions introducing shearing at the droplet surface.

Specifically, we use polystyrene-b-polyethylene diblock copolymers to cover a toluene droplet and float in water towards a flat mica surface. As the droplets approach the mica surface it traps a thin film of water between the buckled drop and the wall. The buckling of the droplet creates a curved interface inside the contact patch. This curvature induces a Laplace pressure which pushes out the trapped fluid over a long period of time. The trapped fluid is drained out through a narrow gap between the mica and the drop and through the long polymer brush. We focus on the late stage drainage oppose to studying the drops' initial approach of the flat wall [57,61,67]. This eliminates the buoyant force from influencing the drainage rate as the drop weight is equilibrated against the wall. Here, we present experimental data and exploit a simple scaling model to describe the drainage rate.

4.2. Experimental Procedure

We use the same emulsion as described in the fluid sessile drop experiment as in chapter 2. The continuous phase was comprised of 60% glycerin to water by weight. A glass cell was filled with continuous phase and was capped by a freshly cleaved mica similar to the sessile drop experiment. Using a micropipette, toluene droplets with excess PS-b-PEO molecules were

released far away from the mica surface. The droplets float up in glycerin/water and rest against a flat sheet of mica. In this study, we utilize two different compositions of PS-b-PEO. Namely, DB1 and DB3 (table 2.1), which are PS32k-PEO11k and PS90k-PEO11k respectively. LSCM was used to image the thin fluid film formed between mica and the drop as a function of time. The high resolution interference data allows us to calculate the shape of the trapped fluid as it changes over time. Nyle red dye was inserted to the toluene phase and was imaged using LSCM to calculate the global drop size.
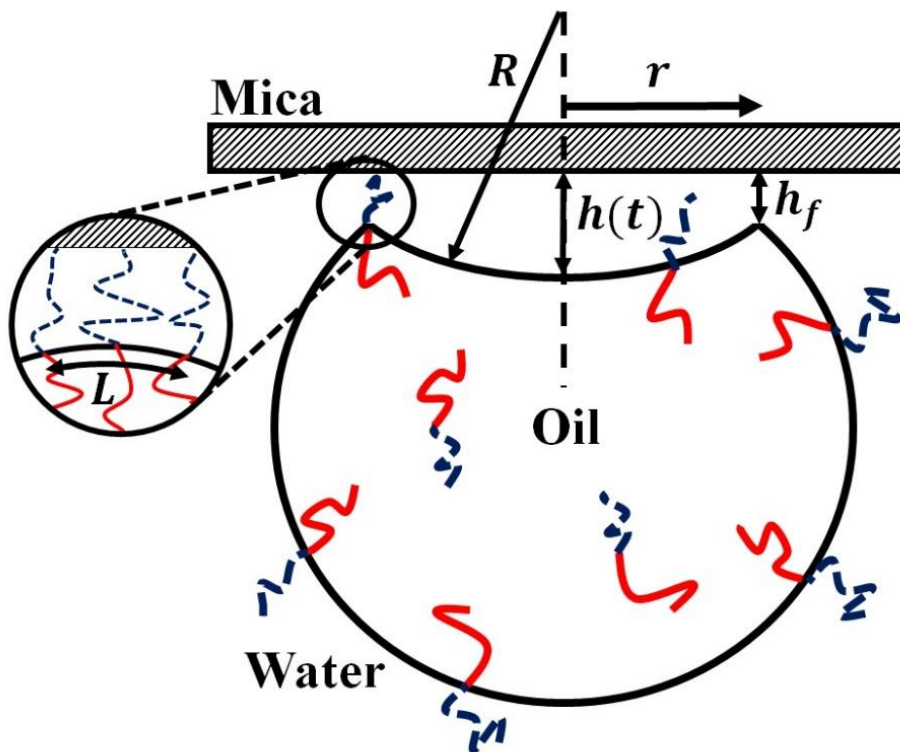
Figure 4.1. Side view schematic of an oil droplet loaded with a diblock copolymer approaching a flat mica surface. Over time the buckled region adjacent to the mica surface slowly flattens as it pushes the water through the thin opening at the droplet contact line.

4.3. Results and Discussion

Deformed droplets were imaged using LSCM and a typical image is shown in figure 4.2 (a). The interference pattern, created by light reflecting off of the mica and the droplet surfaces

55

can be used to construct a high resolution topography of the system. Furthermore, the interference pattern can be captured over time as the fluid drains (Figure 4.2 (b)). Figure 4.3 shows experimental data for the topography of the buckled region inside the contact patch over time. Here, the contact size r of the droplet remains fixed over time and the radius of curvature R increases. The thickness of the contact line which can be seen in the figure 4.2 (b) (first dark ring in the final stage image) represents the distance L (also depicted in figure 4.1). This is the distance which each fluid particle has to move to exit the droplet. A full topography of the buckled region is qualitatively useful (Figure 4.3), however, can be simplified by considering only the film thickness at the center of the cap which we denote as $h(t)$. The height at the center of the film, which is the distance between the mica and the droplet surface was calculated using equation 2.12.
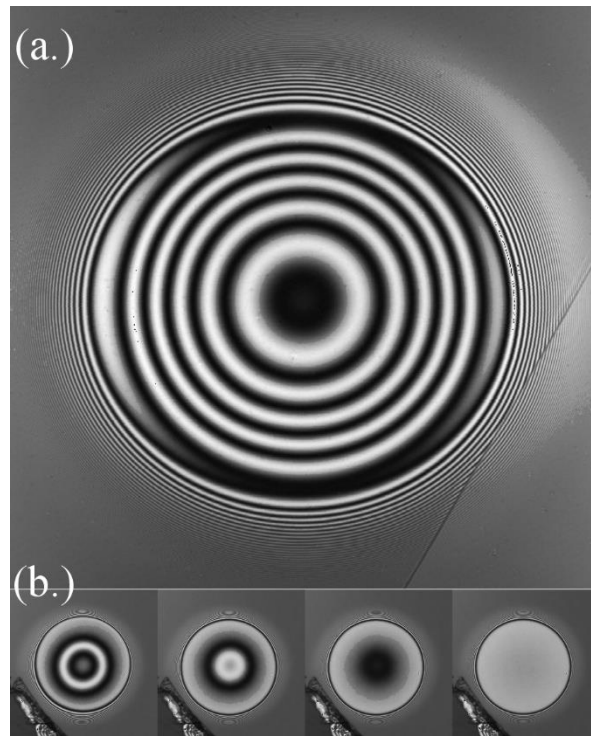
Figure 4.2. (a) LSCM image showing the interference data from light reflected from the mica surface and the droplet surface. (b) The four images captured at different times of the drainage process. Time corresponds to start to ending drainage time, going from left to right.

Figure 4.4 (a) shows the average intensity of a 10 by 10 pixel patch in the center of a typical droplet. To extract, $h(t)$, we used a MATLAB code and fit the intensity to an interference model. A detailed description of the model and how the fit intensity is calculated can be found in appendix B. Calculated $h(t)$ after the fit can be found in figure 4.4 (b).
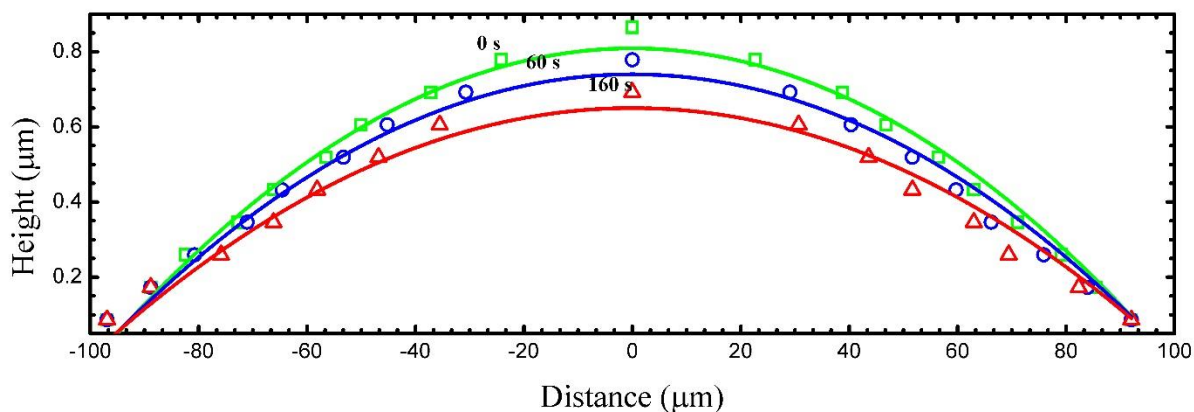
Figure 4.3. Experimental topography of the buckled region of a typical droplet at three separate times (Symbols). The data shown as lines are spherical fits to the data. Note the aspect ratio of the x-axis and y-axis is not 1:1.

The function appears exponential in nature, and notably asymptotically approaches a non-zero thickness h_f. This final height h_f reaches a non-zero value due to the self-assembled PS-PEO brush at the toluene-water interface. Essentially, the interface 'rests' on the PEO brush. The value of h_f is influenced by the size of the polymer and the packing density at the interface. Water is a good solvent for PEO [68,69] and the coils are predicted to be swollen. Similar concentrations (by weight) of polymer to toluene solutions were used for both DB1 and DB3 covered droplets. Note that, although the concentrations were similar by weight, the chain density in each solution is different due to the size of each polymer. The average final height for drained films with DB1 and DB3 was measured to be 22 ± 8.5 nm and 13 ± 5 nm respectively. The trapped pocket of fluid is pushed out through an annular region of width L and height h_f, therefore, the size of the swollen PEO chain is intimately related to the dynamics of the drainage process.

57
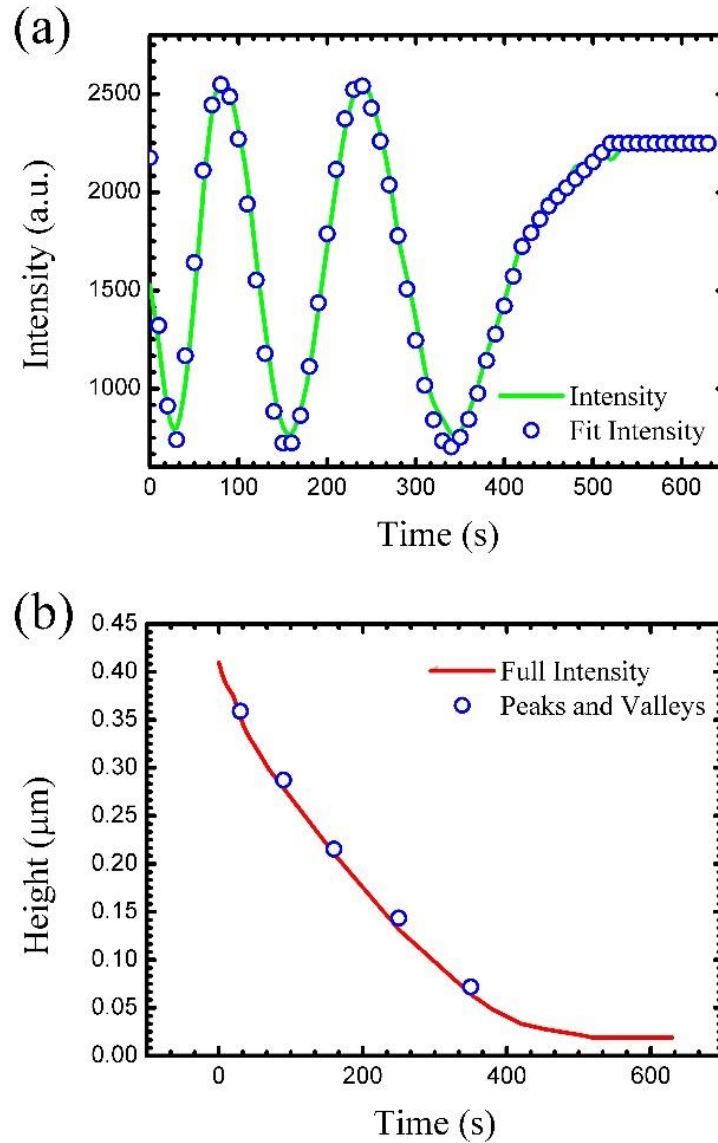
Figure 4.4. (a) Experimental data. The intensity profile at the center of the cap. This is the result of the wave interference between the reflected light from the mica surface and the drop surface. (b) The drainage height over the period of time calculated from the interference data. The circles corresponds to the calculated data points from the peaks and the valleys and the line corresponds to the simulated height using the full intensity.

As the height at the center of the drop appears to drop exponential over time, an exponential fit with a single time constant was used. The draining droplet height was well fit by the exponential function and a single time constant was extracted from each droplet. The time constants for each droplet (for both chain sizes) are presented in figure 4.5. DB1 covered droplet

58

produces a larger time constant τ compared to a similar sized droplet covered with the DB3. This is somewhat a counterintuitive result as the droplet with the larger height (22 nm for the DB1 and 13 nm for DB3) at the rim opening takes longer to drain out. This can be understood better with the introduction of a slip length to the oil-water interface.
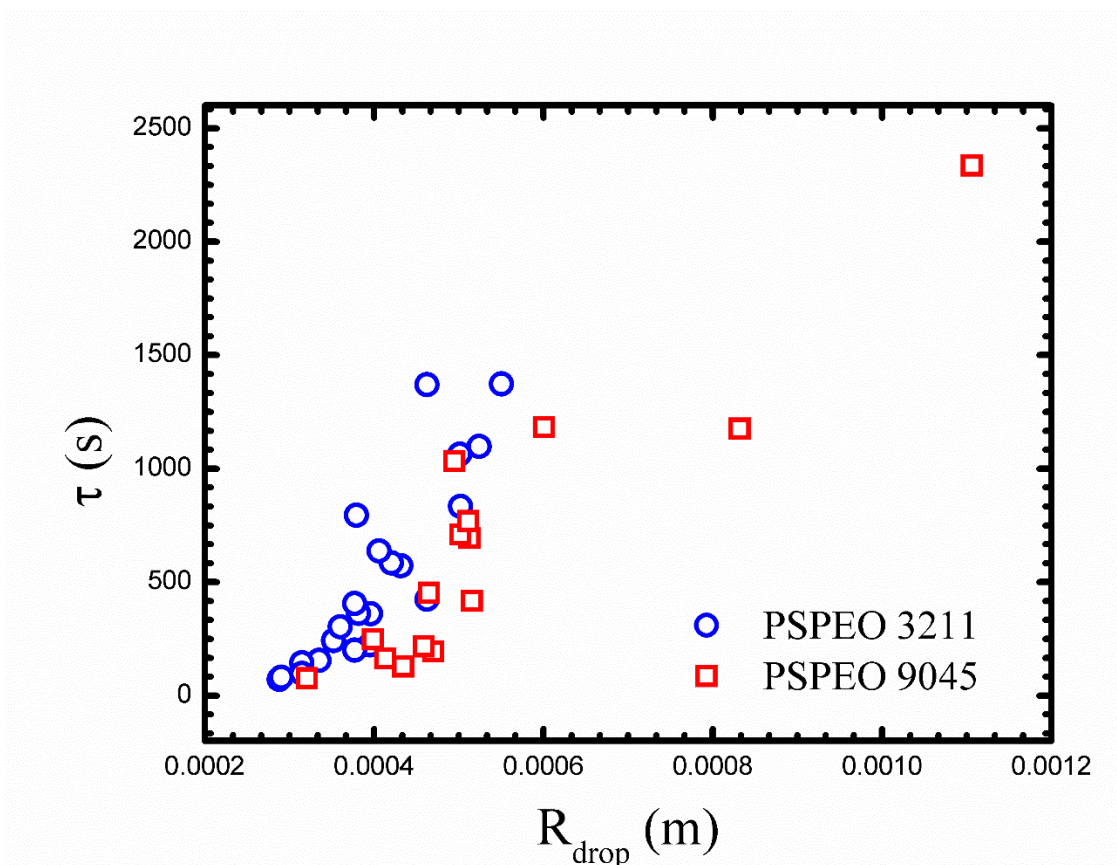
 Figure 4.5. Experimentally extracted single time constants from exponential fits for an ensemble of droplets with drop size R_{drop}. Note that for similar size drops, DB1 covered drops drain out slower than the DB3 covered droplets.

4.3.1. Drainage Scaling

When the polymer stabilized emulsion droplet approaches the flat mica surface, it buckles forming a spherical indentation which eventually traps a pocket of fluid from the continuous (water/glycerine) phase. The continuous phase flows out through a narrow opening at the contact

59

line with a height of h_f and a width of L. We model the late stage drainage with the well-known Navier-Stokes equation under the lubrication approximation [6];

$$-\frac{\partial P}{\partial x} + \frac{1}{\eta}\frac{\partial^2 v}{\partial z^2} = 0. \tag{4.1}$$
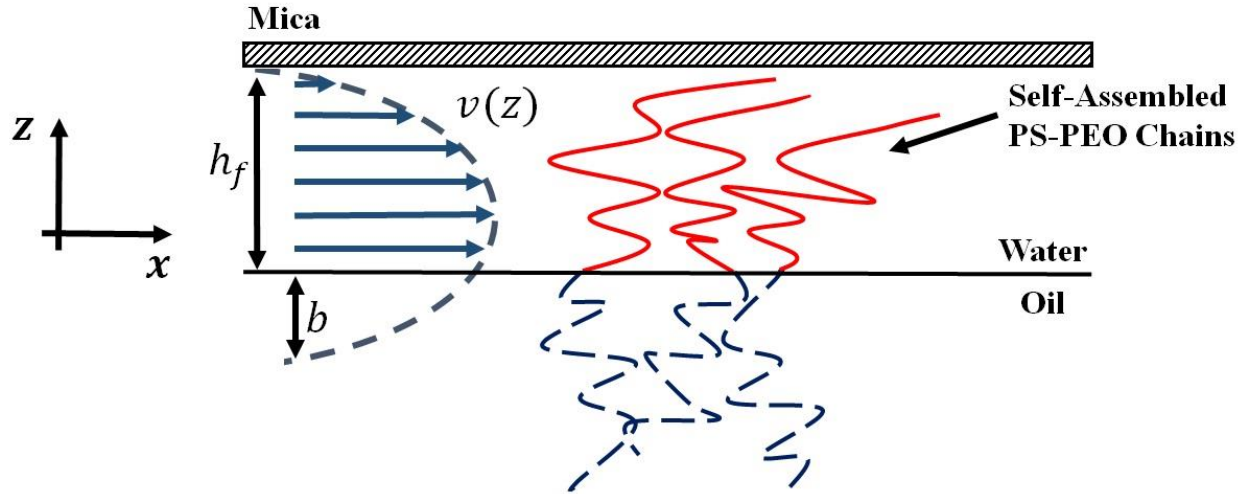
Figure 4.6. A schematic representation of the velocity profile with a slip length at the oil water interface. Note, the oil-water surface at the point at which the fluid is forced out through the polymer brush has curvature which is not shown in the figure.

Here η is the dynamic viscosity and P is the pressure driving the flow. Equation 4.1 can be solved by two successive integration with respect to the z coordinate. This produces the parabolic velocity profile,

$$v_x(z) = \alpha z^2 + \beta z + \delta, \tag{4.2}$$

which can be solved using the two boundary conditions; 1) velocity at the solid mica surface is zero and 2) velocity at the oil-water interface is $v_0 = bv'$ where b is the slip length and v' is the x derivative of v_x. The result is a velocity in the form;

$$v_x(z) = \left(\frac{1}{2\eta}\frac{dP}{dx}\right)\left[(z^2 - zh_f) - \left(\frac{bh_f^2}{h_f + b}\right)\left(1 - \frac{z}{h_f}\right)\right] \tag{4.3}$$

The velocity profile allows us to calculate the volumetric flow, Q;

60

$$Q = \frac{\pi r h_f^3}{\eta}\left(-\frac{\partial P}{\partial x}\right)\left[\frac{1}{3} + \frac{b}{h_f}\right]. \tag{4.4}$$

The trapped fluid forms a contact patch of radius r and radius of curvature R (Figure 4.1). The droplet has a non-zero surface tension, therefore, the curvature of the buckled region induces a Laplace pressure which drives the fluid out:

$$\left(-\frac{\partial P}{\partial x}\right) \sim \frac{2\gamma}{RL}. \tag{4.5}$$

The surface tension of the PS-PEO stabilized toluene glycerin/water interface is γ and L is the (rim width) length over which the pressure drops. The droplet surface is assumed to have a uniform surface tension throughout the draining period, which we measure independently via the sessile drop method [28,35,70] and pendant drop method [36].

Justified by our observations, we assume that the buckled region remains spherical throughout the drainage. The geometry of the trapped spherical cap can be used to relate the radius of curvature R to the time dependent h and the contact patch size r as $R = r^2/2h$. Hence, the flow rate in Eqn. 4.4 becomes:

$$Q \propto \frac{h_f^2 b\gamma}{rL\eta} h \tag{4.6}$$

As shown in figure 4.3, the curvature R changes over time while the size of the contact patch, r remains constant. Hence, the volume of the trapped fluid (spherical) can be written as:

$$V \sim \pi h(r^2 + h^2). \tag{4.7}$$

Note that the only time dependent variable in equation 4.7 is the height h. Therefore, the time derivative of V can simply relate to the above derived volumetric flow rate Q as:

$$Q = \frac{dV}{dt} \sim r^2 \frac{dh}{dt}. \tag{4.8}$$

Combining equation 4.6 and equation 4.8 provides the governing equation for the height at the center of the draining cap as

$$\frac{dh}{dt} \sim \frac{h_f^2 b \gamma h}{r^3 L \eta_{eff}}. \tag{4.9}$$

The solution for equation 4.9 is

$$h(t) \sim e^{-\frac{t}{\tau}}, \tag{4.9}$$

where $\tau = \frac{r^3 L \eta}{h_f^2 b \gamma}$.
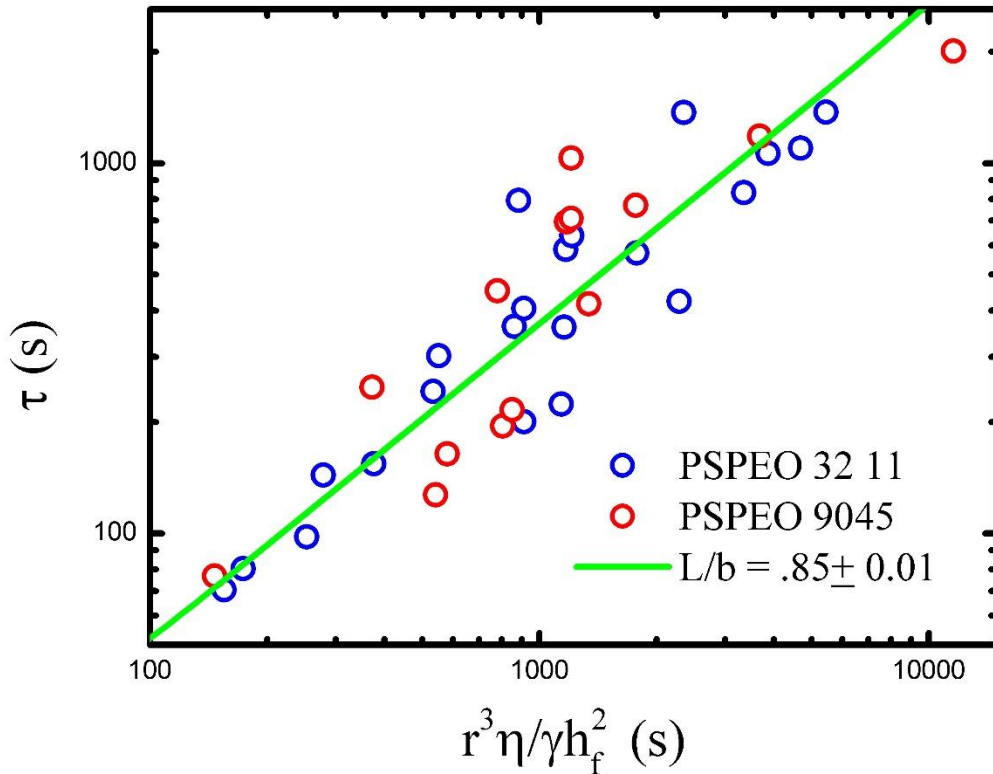
Figure 4.7. Experimentally extracted time constants against the other variables leaving the ratio L/b as the slope. r and h_f were experimentally measured using LSCM, γ was measured using the sessile drop method. A linear fit produces the slope, $L/b = 0.85 \pm 0.001$.

62

Figure 4.7 shows τ as a function of all the variables in the time constant with the exception of the ratio L/b for ensembles of DB1 and DB3 covered droplets. The surface tension was experimentally calculated using the sessile drop technique (from chapter two) to be $\gamma = 10 \pm 2$ mN/m and 35 ± 5 mN/m for DB1 and DB3 covered drop interfaces respectively. The dynamic viscosity of 60% glycerin in water at room temperature was quoted as $\eta = 0.0108$ Pa.s. [31,32]. The ensemble is fit with $L/b = 0.850 \pm 0.001$.

We expect the slip length b for a polymer covered interface to be in the order of nanometers [71]. The L/b fit in figure 4.7 is approximately one, which shows that the rim width L is comparable to the slip length. LSCM images are also indicative of a small L as the ring is represented by only a few pixels.

4.4. Summary

Here, we have produced a much different interface compared to those used in other slip length experiments [71-73]. 1) Our interface remains fluid-fluid with self-assembled long diblock copolymers whereas other experiments use end grafted polymer on a solid surface and 2) our flow channel heights are comparable to the chain length. Typical parallel plate rheometery experiments have flow channel height much longer than the polymer length [71-73]. We use LSCM to image an oil droplet covered with PS-PEO diblock copolymer molecules approaching an atomically flat mica surface under water. Simple hydrodynamics affects the interaction between the mica and the oil droplet, buckling the droplet and trapping a small amount of water between the wall and the droplet. The trapped volume of water is pushed out through a narrow brushy gap. The flow is driven by the Laplace pressure created by the curved interface at the buckled region. We find different drainage rates as the size of the polymer brush is changed. Motivated by the lubrication

approximation, a simple scaling model predicts the ratio between the rim width and the slip length

of the oil-water interface.

5. THE INFLUENCE OF DIBLOCK COPOLYMER ON FLUID-FLUID INTERFACES

5.1. Introduction

The focus of this chapter is to experimentally study the physics of diblock copolymer self-assembly at oil-water interfaces in sessile droplets. This work builds on the experiments conducted in the previous chapters. We use polystyrene-b-poly(ethylene oxide) (PS-PEO) molecules of several different sizes and concentrations to investigate their structure at an oil-water interface for different sized emulsion droplets. The thickness of the outer polymer brush (PEO) was experimentally measured with laser interference (chapter 4) and the surface tension for a range of PS-PEO concentrations were measured using the sessile drop technique (Chapter 2). We see a decrease in surface tension of the oil-water interface as the PS-PEO concentration is increased and a PEO brush height increase as the concentration is increased. The experimental data are presented empirically and the trends in the data are qualitatively described.

5.1.1. Properties of Amphiphilic Polymers

In chapter 1 the random walk model and the Flory's theory was discussed. In section 2.1.1., amphiphilic polymers were introduced. Here, we combine the amphiphilic polymers and single chain statistics to discuss the dynamics of an amphiphilic polymer chain. An amphiphilic polymer is a polymer which has both hydrophobic and hydrophilic properties. Most hydrophobic chains are made of aliphatic compounds $(CH_3[CH_2]_n)$ and the hydrophilic chains are ionic (anion or cation). Hydrophilic chains can also be neutral in charge and be soluble in water. Poly(ethylene-oxide) is a good example for this type where the monomer has the type $(-CH_2 - CH_2 - O-)$ [5].

5.1.1.1. Hydrophilic-lipophilic balance

Some amphiphilic polymers are soluble in both the oil phase and water phase. In order to better utilize these polymers, the amphiphilic properties need to be characterized. For example it is important to measure if an amphiphilic polymer is more soluble in oil phase or water, because at equilibrium some of the polymer chains will be in the water phase and others in the oil phase. The ratio between the concentration of polymer in oil c_o and the concentration of polymer in water c_w is

$$\frac{c_o}{c_w} = k, \tag{5.1}$$

where k is the segregation coefficient. If k is greater than one, the polymer is more hydrophobic and if k is less than one, the polymer is more hydrophilic. There are many downfalls in the classification, one of which is, if the polymer is either extremely hydrophobic or hydrophilic, measuring k becomes almost impossible.

Therefore, another way of characterizing the amphiphilic properties were introduced by Griffin in 1949 [77]. It is described as the hydrophilic-lipophilic balance (HLB). This defines whether the molecule is more soluble in the oil phase or the water phase. Briefly, the HLB classification is as follows; if the work done by moving a chain from water to oil is Δ, the segregation coefficient can be defined as

$$k = e^{\left(\frac{-\Delta}{KT}\right)}, \tag{5.2}$$

where K is Boltzmann constant and T is temperature. Δ can be expressed as

$$\Delta = U_h n_h - U_l n_l, \tag{5.3}$$

where U_h is the energy that is required to transfer one hydrophilic unit from water to oil and n_h is the number of hydrophilic units in a chain. Similarly, U_l is the transfer energy of one hydrophobic

unit and n_l is the number of such units in a chain. The hydrophilic-lipophilic balance, then becomes the negative logarithm of the segregation coefficient ($HLB = -\log_{10} k$) and can be rewritten as

$$HLB = 7 + \alpha(m_h n_h - m_l n_l), \tag{5.4}$$

where m_h and m_l are phenomenological coefficients [5]. α is the normalization constant and chosen to make the HLB values fall in the range of 0 to 20. Here, zero corresponds to completely lipophilic and 20 corresponds to completely hydrophilic (see figure 5.1). HLB value of 7 is arbitrarily assigned to represent the neutral agents where segregation constant k is one. This is done in analogy to the pH values (where neutral solvents has a pH of 7).
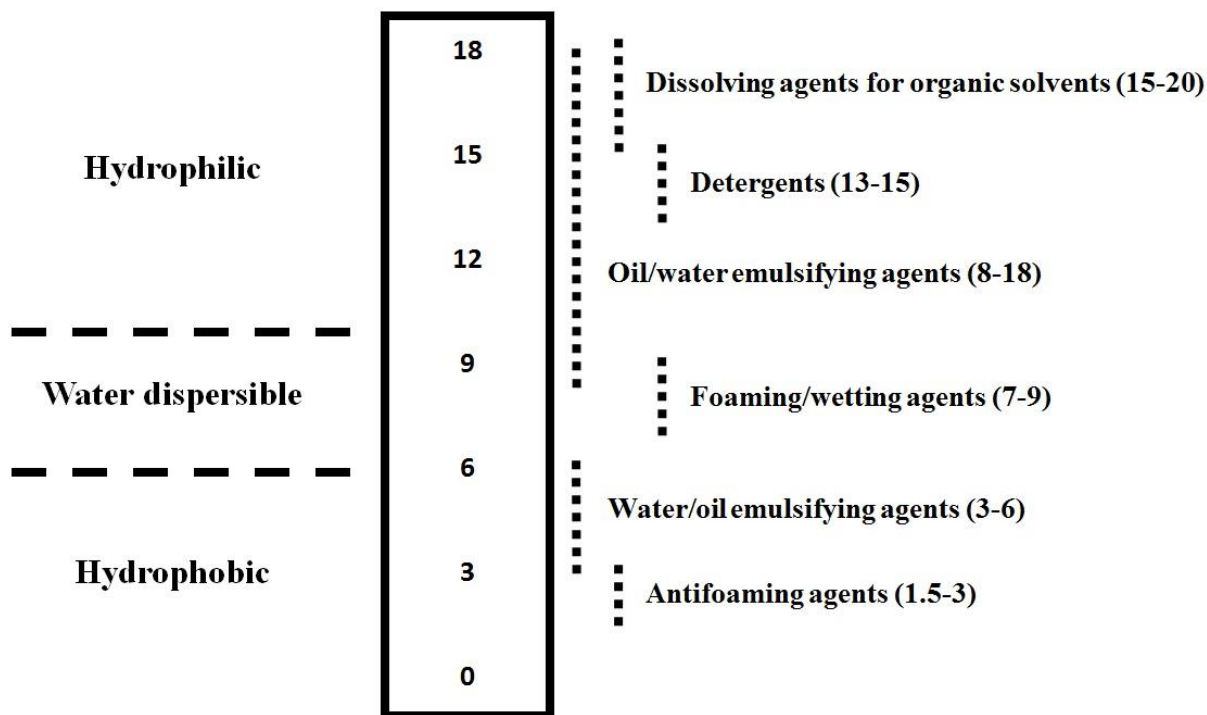
Figure 5.1. HLB index for different categories of surfactant agents. The data was adapted from [5] and represented graphically.

5.1.1.2. Solubility parameter

Intermolecular interaction of materials can also be characterized using the solubility parameter (δ). Theoretically, the solubility parameter can be used to verify the calculated HLB

values for an amphiphilic molecule or it can be used to describe the amphiphiles which are not described by HLB values. The solubility parameter was introduced by Hilderbrand [78] which describes the overall attractive forces between neighboring molecules in a condensed phase. The cohesive energy density is characterized by the solubility parameter as

$$\delta = \sqrt{\frac{\Delta H_v + RT}{V_m}},$$ (5.5)

where $\Delta H_v + RT$ is the enthalpy of vaporization and V_m is the molar volume. As the cohesive energy density is increased the adjacent molecules are tightly attracted to one another. The closer the solubility parameter of two materials, higher the miscibility of the two materials. For example, water has a δ of 47.9 $(Jcm^{-3})^{0.5}$ whereas diethyl ether has a δ of 15.1 $(Jcm^{-3})^{0.5}$ and therefore, these are immiscible [78]. Similarly, The solubility parameter can be used to find the optimum surfactant for stabilizing a particular oil/water phase. The solubility parameter for some commonly used solvents are presented in table 5.1.

Table 5.1. δ values of commonly used solvents an materials [79] in $[(Jcm^{-3})^{0.5}]$.

Material	δ	Material	δ
Chloroform	19.0	Toluene	18.2
Ethanol	26.5	Styrene	19.0
1-Propanol	24.5	Ethylene Glycol	61.2
Glycerol	33.7	Water	47.9

5.1.1.3. Statistical Mechanics Approach

A block copolymer at the oil-water interface can be described using configurational statistical mechanics similar to the lattice model introduced for a simple random walk. Let us consider for simplicity, a single polymer chain consisting of A segments followed by B segments

68

at an oil-water interface. Here, we consider excluded volume chains with each lattice site occupied by either polymer segment A, segment B, solvent molecule C or B (see figure 5.2). Similar to the Flory-Huggins free energy [74,75], we can write down the free energy for the block copolymer as

$$F = E - TS, \tag{5.6}$$

where E is the interaction energy between the segments and solvent molecules and S is a sum of the conformational entropy and the translational entropy (mixing entropy).
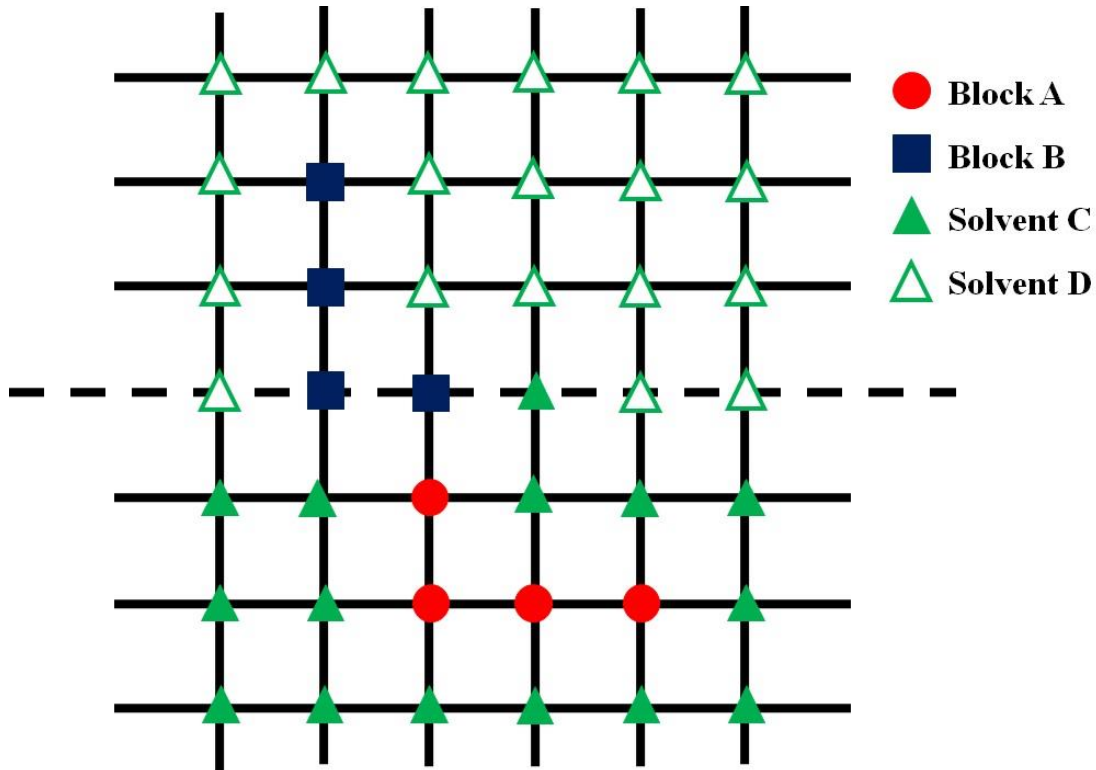
Figure 5.2. Lattice model for a block copolymer (excluded volume) at an oil-water interface.

For simplicity, the interaction energy E only consists of pair interactions between the nearest neighboring lattice sites. Let us assume that the interaction energy between these 4 molecules (using the mean field approximation) as ϵ_{AA}, ϵ_{BB}, ϵ_{CC}, ϵ_{DD}, ϵ_{AB}, ϵ_{AC}, ϵ_{AD}, ϵ_{BC}, ϵ_{BD}, ϵ_{CD}. We can measure the composition of the mixture as a volume fraction φ (i.e., the volume fraction of A segments φ_A is defined as the number of sites occupied by A segments divided by

the total number of lattice sites). The total volume of the system is then, $\varphi_A + \varphi_B + \varphi_C + \varphi_D = 1$.
We assume that a particular site has $z\varphi_A$, $z\varphi_B$, $z\varphi_C$, $z\varphi_D$, A, B, C, D, neighbors respectively. The
total interaction energy can be written using these assumptions as

$$
E = \frac{z}{2}[(\varphi_A^2 - \varphi_A)\varepsilon_{AA} + (\varphi_B^2 - \varphi_B)\varepsilon_{BB} + (\varphi_C^2 - \varphi_C)\varepsilon_{CC} + (\varphi_D^2 - \varphi_D)\varepsilon_{DD} \tag{5.7}
$$
$$
+ 2\varphi_A\varphi_B\varepsilon_{AB} + 2\varphi_A\varphi_C\varepsilon_{AC} + 2\varphi_A\varphi_D\varepsilon_{AD} + 2\varphi_B\varphi_C\varepsilon_{BC} + 2\varphi_B\varphi_D\varepsilon_{BD}
$$
$$
+ 2\varphi_C\varphi_D\varepsilon_{CD}].
$$

Unlike for the two molecule system, here, it quickly becomes too complicated to introduce a single
dimensionless parameters χ [74,76].

The mixing entropy S can be written using Boltzmann formula [76] as

$$
S = -k_b(\varphi_A \ln \varphi_A + \varphi_B \ln \varphi_B + \varphi_C \ln \varphi_C + \varphi_D \ln \varphi_D). \tag{5.8}
$$

Here, it is assumed that neighboring sites are independent of each other. If a site is occupied by a
particular molecule, it makes neither more or less probable that a neighboring site is similarly
occupied. The total free energy of the system can now be written combining E and S.

5.2. Experimental Procedure

This is an extension of the work done in the previous chapter. A brief discussion of the
experimental procedure presented in this section. A glass cell was filled with 60% glycerin in
water, capped with a freshly cleaved mica and toluene droplets (with the diblock copolymer PS-
PEO) were created using a micropipette. Two different molecular weights of PS-PEO were used
in this experiment (DB1 and DB3 from table 2.1). 0.05% DB3 and DB1 to toluene by weight was
prepared to compare the chain size effects. Several other concentrations of DB1 to toluene (by
weight) were used to control the number of polymer chains at the oil-water interface (table 5.2).
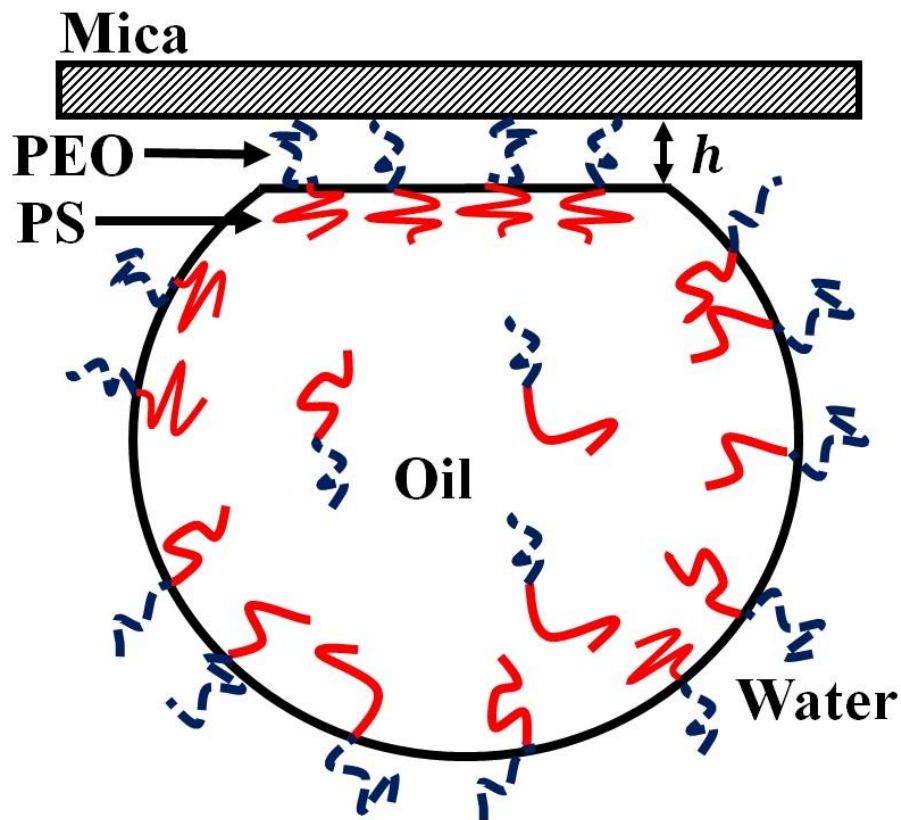
Figure 5.3. A schematic presentation of PS-PEO covered oil droplet in water.

All drops were imaged in 3D using laser scanning confocal microscopy (LSCM with 488 nm wavelength). Olympus microscope lenses of several different magnifications were used (5X, 10X, 50X and 100X). High resolution interference data (figure 2.8. and 2.9.) was used to calculate the shape near the contact region. Nile red dye was mixed into toluene to capture fluorescence in order to measure the size of each droplet.

5.3. Results and Discussion

Ensemble of DB1 (PS_{32k}-PEO_{11k}) covered toluene droplets with a range of drop sizes ($50 - 1000 \ \mu m$) were imaged using LSCM. The experimentally measured $R(r)$ data are presented in figure 5.4 (a).
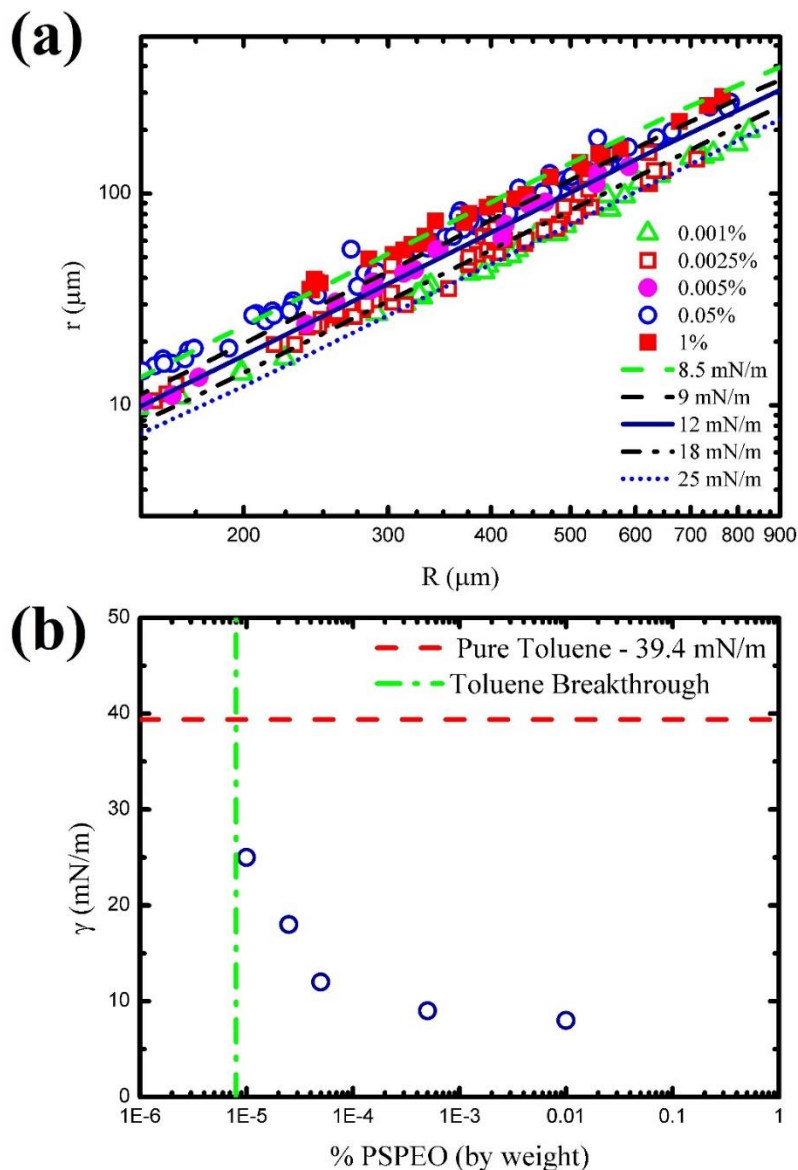
Figure 5.4. (a) Experimental $R(r)$ data for a range of concentrations of PS_{32k}-PEO_{11k} to toluene. These are well fit with surface tension curves calculated using sessile drop geometry (Bashforth and Adams – Chapter 2). (b) Interfacial surface tension for each concentration. Bare toluene-60% glycerin/water surface tension was experimentally measured using the pendent drop technique.

The experimental $R(r)$ data were well fit with Bashforth-Adams surface tension curves.

The surface tensions of each concentration of DB1 are also presented in table 5.2. The pendent

drop technique was used to measure the surface tension of toluene to 60% glycerin/water interface

and was found to be $39.4 \pm 1.5 \, mN/m$. Ideally, the surface tension of the interface reaches an upper limit of this value as the polymer concentration is reduced. However, as the PS-PEO concentration is reduced below 0.001% (by weight), the toluene breaks through the polymer brush and wets the mica surface (see figure 5.5).
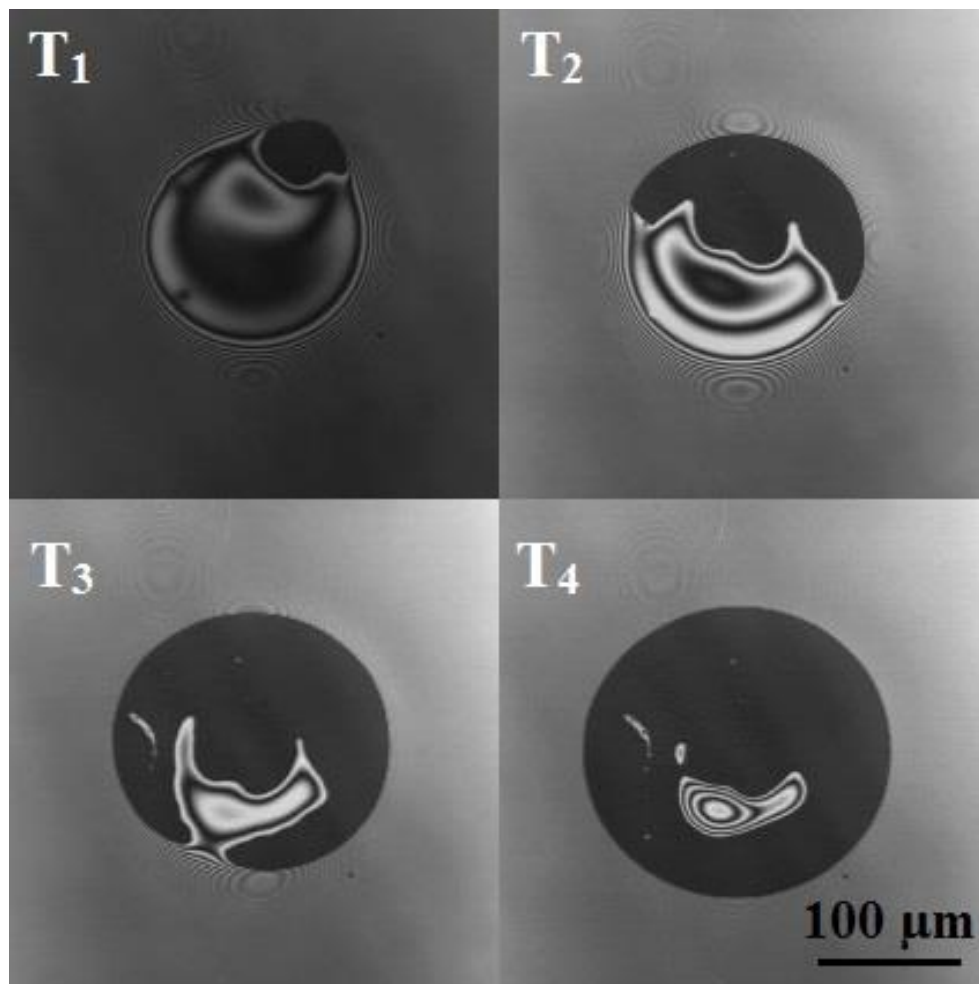
Figure 5.5. Confocal micrograph of the contact patch of a toluene drop containing 0.001% PS-PEO (3211) by weight in 60% glycerin/water. T_1-T_4 corresponds to the time increment of the toluene breakout and wetting the mica.

Table 5.2. DB1 concentration to toluene by weight.

Name	Concentration	γ (mN/m)	Name	Concentration	γ (mN/m)
C1	0.001	25 ± 1	C6	0.05	9 ± 1
C2	0.0025	18 ± 1	C7	1	8.5 ± 1
C4	0.005	12 ± 1	C8	0.7	$-$
C5	0.01	$-$			

The interfacial tension (of toluene-water) was decreased as the PS-PEO concentration was increased. Higher concentrations of PS-PEO solutions yield a critical surface tension of 8.5 mN/m. At higher concentration the interface becomes saturated with PS-PEO chains. At these concentrations, the energy cost of moving a molecule from the bulk to the interface becomes greater than the interfacial energy reduction from a single chain. Therefore, an equilibrium concentration at the interface is reached which balances the enthalpy and the entropy of the molecules.

The heights of the PEO brush (outer brush thickness of the droplet) were measured using the same technique used in the drop drainage experiments of chapter 4. Briefly, the intensity of the draining drop at the center was well fit with the intensity model (Appendix B) and the final thickness measurement is calculated using the final intensity at the center of the droplet. Experimentally measured outer brush heights (h) for a range of concentrations are presented in figure 5.6.
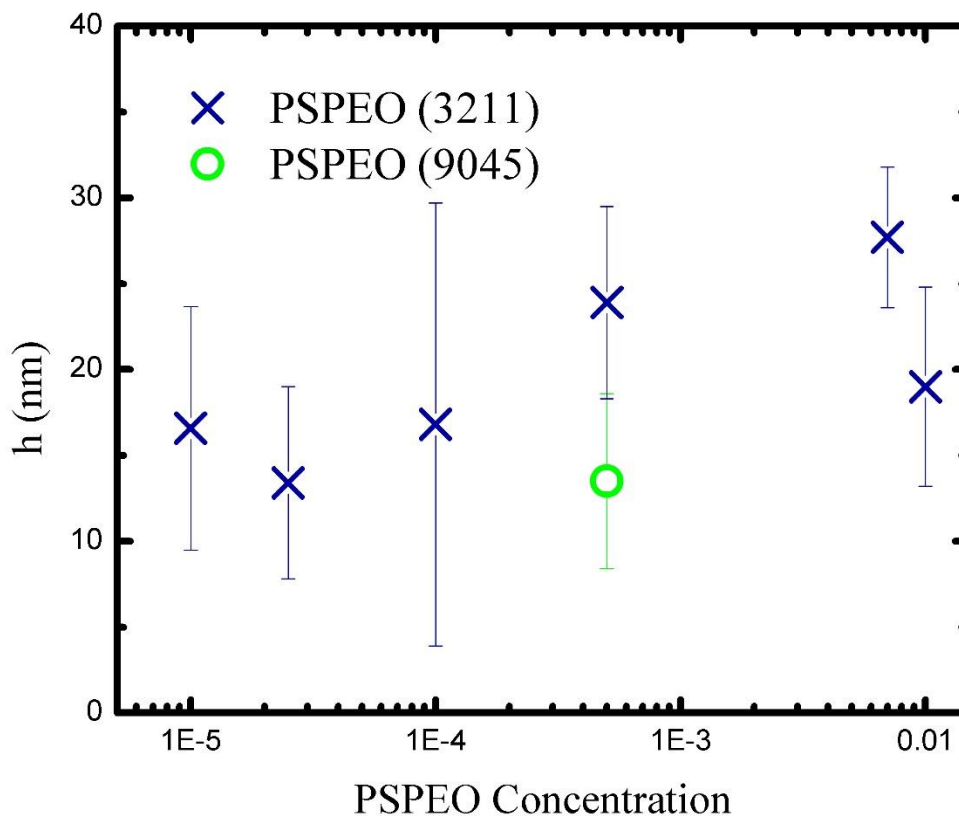
Figure 5.6. Experimentally measured PEO brush thickness h for a range of concentration. Circular point represents the DB3 brush height and the 'X' points represent the DB1 brush height.

There are 2 important observations from this figure, 1) at the same PS-PEO concentration (by weight to toluene), PS-PEO with the larger molecular weight (DB3) has a smaller brush length compared to the PS-PEO with a smaller molecular weight (DB1) and 2) PEO brush height increases as the polymer concentration is increased (for DB1). Below, we present a qualitative argument to describe the behavior of the PS-PEO packing at the interface.

The concentration of polymer to toluene by weight does not fully describe the chain density at the interface. Typically, Langmuir adsorption equation or Szyszkowski equation is used to calculate the surfactant surface density [80-82]. However, as the molecule becomes larger

compared to traditional surfactant molecules, these values are no longer accurate. The free energy for a single diblock copolymer at an interface can be written as described in section 5.1.1.3. However, the free energy changes considerably as more molecules are introduced to the interface. The problem can be simplified by writing down the free energy at the interface as

$$f = f_{PS} + f_{PEO},$$ (5.9)

where f_{PS} includes the contributions of PS chains to the free energy and f_{PEO} includes the contributions from PEO chain to the free energy[83,84].

Let us start by describing the behavior of PS-PEO chains in the experiment. An oil/water emulsion is created by depositing a toluene droplet with PS-PEO chains in a large pool of water. PEO molecules drive the diblock copolymers to the oil-water interface due to their thermodynamic interactions. As quoted in table 5.1 the solubility parameter of PEO (61.2 $(Jcm^{-3})^{0.5}$) is closer to that of water (47.9 $(Jcm^{-3})^{0.5}$) than toluene (18.2 $(Jcm^{-3})^{0.5}$). At the interface a monolayer of the diblock copolymer is created with the PEO chain in the water phase and the PS chain in the toluene phase. PS is a highly hydrophobic molecule with low HLB values and PEO has HLB values ranging from 9 to 16 depending on the molecular weight of the PEO chain [85,86]. The interaction energy of the PS does not change as it does not transfer to a different solvent. Therefore, the only interaction energy contribution to the free energy is the PEO/water and PEO/toluene.

As the concentration of the polymer in the bulk is increased, more chains are driven to the interface due to thermal fluctuations, diffusion and entropy. However, we lose conformational entropy as the chains become more confined by neighbors on the interface. In this experiment, we have used PS-PEO chains with a larger PS side compared to PEO (both DB1 and DB3). Therefore, the average spacing per chain at the interface is dominated by the PS side. The entropic loss due to chain confinement is greater on the PS side. This contribution to the free energy at the interface

76

drives the molecules back to the bulk phase. Furthermore, the PS chains stretches more as the surface chain density increases. This stretching energy is the other negative contribution to the free energy of the interface.
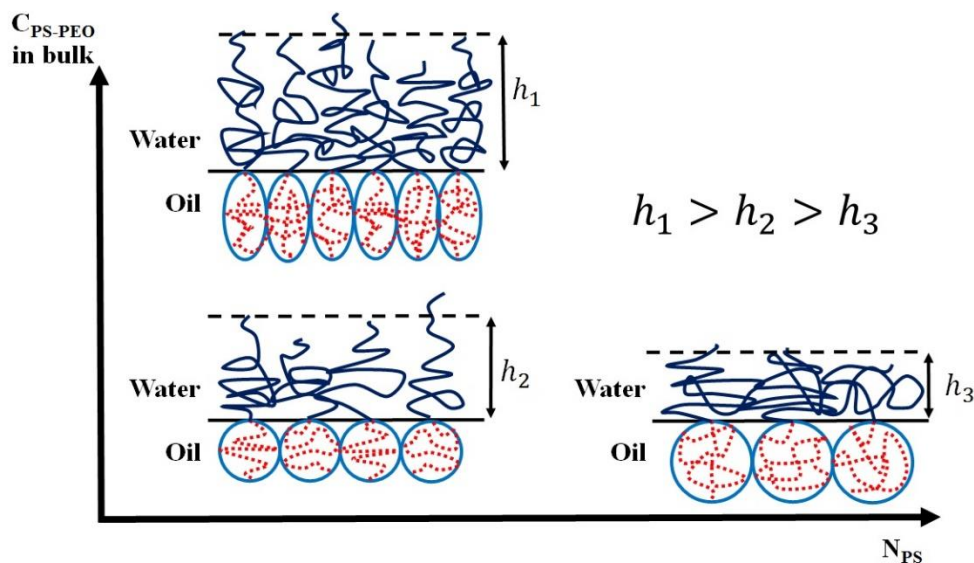
Figure 5.7. Schematic representation of adsorbed diblock copolymer at the oil-water interface qualitatively showing the height changes the chain density at the interface is increased and the size of PS is changed.

The experimental results presented in figure 5.6, show that the PEO brush height increases as the bulk concentration is increased. However, at a certain critical (bulk) concentration, the number of chains which can be packed at the interface is maximized. In other words, it costs more energy to add a molecule to the interface than for its PEO segment to be in the oil phase. Therefore, increasing bulk concentration no longer changes the PEO height. At the lower concentration end, the PEO brush height reaches another critical thickness. Here, the PEO brush adopts a statistical chain length of a polymer in a good solvent ($\frac{a}{\sqrt{6}}N^{3/5} = 17.9\ nm$) [3,4,76]. The experimentally measured PEO brush height for 0.001% PS-PEO is $16.6 \pm 7.1\ nm$. Although the error in the experimental measurement is high, it is close to the scaling prediction.

As the size of PS is increased, we can see from figure 5.6 that the PEO brush height is decreased. This indicates that there is more space in the lateral direction for the PEO brush to move before it sees another PEO monomer. Therefore, the height of the PEO brush is decreased.
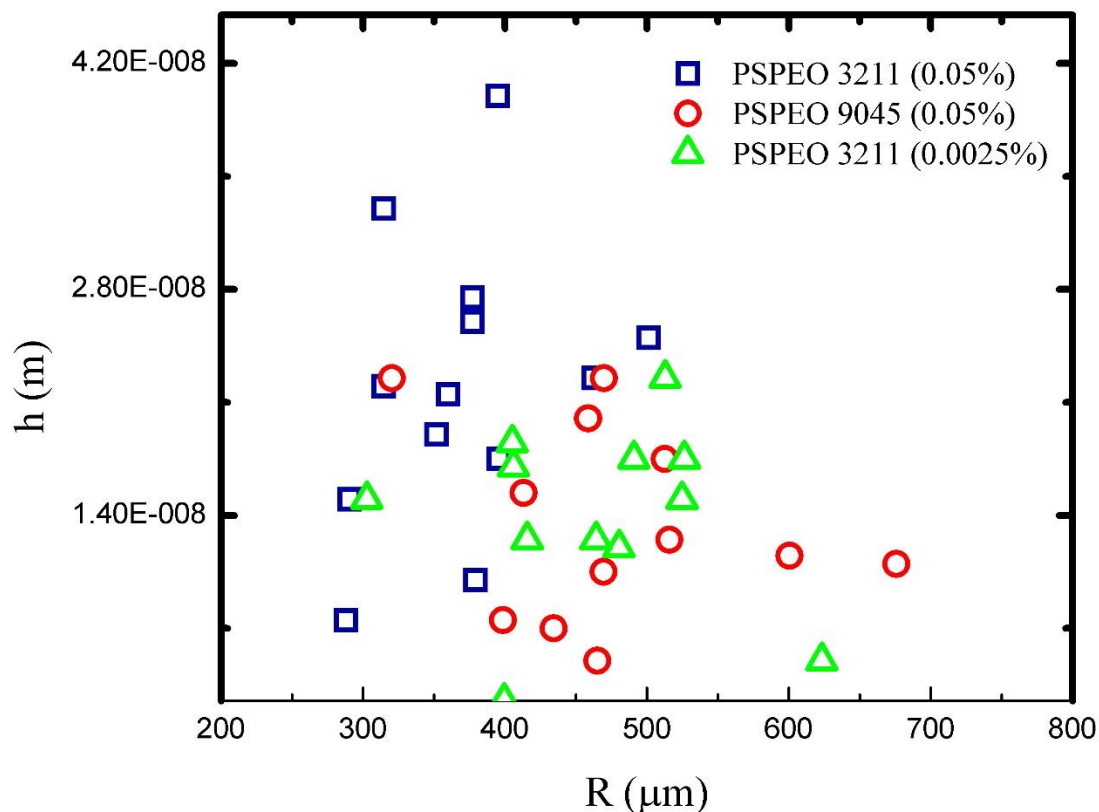
Figure 5.8. Experimentally measured PEO brush height for an ensemble of droplets from two different sizes of PS-PEO chains and for a different concentration of PS-PEO (32-11) chain.

Another important variable in calculating the PEO brush height is the weight of the emulsion drop. PEO brush heights for an ensemble of droplets are presented in figure 5.8. Here, we find no trend suggesting a correlation between the PEO brush height and drop size. If the number of chains at the interface remains constant as the size of the emulsion drop is increased, we should expect the increased weight to and add more pressure per chain. Hence, the brush height

should be reduced. We do not see a noticeable change in the height as the drop size is increased, therefore, the weight per chain must not be a significant contribution to the chain conformation.

5.4. Summary

Toluene droplets (with PS-PEO chains in the toluene phase) were created in glycerin/water mixture and were imaged using LSCM. It was found that as the PS-PEO concentration is increased, the oil-water surface tension was reduced until a critical surface tension was achieved. At a particular critical concentration, the interface reached a maximum chain packing density. PS-PEO chains are transported to the oil-water interface due to enthalpic interactions. Laser interference micrographs were used to measure the PEO brush height at the interface. The bulk concentration effects were measured for a particular PS-PEO chain size. For lower concentrations of PS-PEO, the height of the PEO brush begins at a critical height and can be described using the statistical chain length for a polymer in a good solvent (PEO in water). As the concentration is increased, the PEO brush height increases until it reaches another critical height. This is imposed by the balance between entropy and enthalpy where adding a molecule to the interface costs more energy than the molecule being in the bulk.

The PEO height was measured for a larger PS-PEO brush and was compared to the original molecule at the same bulk concentration. Although the bulk concentrations remain the same, the number of molecules at the interface is changed due to the change in spacing per molecule. Therefore, the PEO brush has more lateral space to move before it finds another PEO molecule. Hence, the PEO brush height was decreased for the chain consisting of the larger PS side. Furthermore, the emulsion drop size effects on PEO height were studied. We find no trend in suggesting a change in brush height for either of the PS-PEO (DB1 or DB3) molecule.

REFERENCES

[1]   H. R. Allcock, *Introduction to Materials Chemistry* (Willey, Hoboken, NJ, 2008).

[2]   M. Rubinstein and R. Colby, *Polymer Physics* (Oxford University Press, 2003), 1 edn.

[3]   U. W. Gedde, *Polymer Physics* (Chapman & Hall, London, UK, 1995).

[4]   P.-G. de Gennes, *Scaling Concepts in Polymer Physics* (Cornell University Press, Ithaca, New York, 1979).

[5]   P.-G. De Gennes, F. Brochard-Wyart, and D. Quere, *Capillarity and Wetting Phenomena - Drops, Bubbles, Pearls, Waves* (Springer, 2004).

[6]   L. D. Landau and E. M. Lifshitz, edited by J. B. Sykes, and W. H. Reid (Elsevier Butterworth Heinmann, 1987).

[7]   D. E. Discher and A. Eisenberg, Science **297**, 967 (2002).

[8]   R. Langer, Science **249**, 1527 (1990).

[9]   A. S. Utada, E. Lorenceau, D. R. Link, P. D. Kaplan, H. A. Stone, and D. A. Weitz, Science **308**, 537 (2005).

[10]   B. M. Discher, Y. Y. Won, D. S. Ege, J. C. M. Lee, F. S. Bates, D. E. Discher, and D. A. Hammer, Science **284**, 1143 (1999).

[11]   H.-Y. Chang, Y.-J. Sheng, and H.-K. Tsao, Soft Matter **10**, 6373 (2014).

[12]   I. Wyman, G. Njikang, and G. Liu, Progress in Polymer Science **36**, 1152 (2011).

[13]   V. D. Gordon, C. Xi, J. W. Hutchinson, A. R. Bausch, M. Marquez, and D. A. Weitz, Journal of the American Chemical Society **126**, 14117 (2004).

[14]   A. J. Hyde, D. M. Langbridge, and A. S. C. Lawrence, Discussions of the Faraday Society, 239 (1954).

[15]   W. B. Tucker, Massachusetts Institute of Technology, 1938.

[16]   C. E. Stauffer, Journal of Physical Chemistry **69**, 1933 (1965).

[17]   J. M. Andreas, E. A. Hauser, and W. B. Tucker, Journal of Physical Chemistry **42**, 1001 (1938).

[18]   T. Young, Philosophical Transactions of Royal Society of London **95**, 65 (1805).

[19]   P. S. Laplace, *Mécanique céleste* (Hillard, Gray, Little, and Wilkins, Boston, 1806).

[20]   R. P. Rand, Biophysical Journal **4**, 303 (1964).

[21]   E. A. Evans and R. Waugh, Biophysical Journal **20**, 307 (1977).

[22]   E. Evans and W. Rawicz, Physical Review Letters **64**, 2094 (1990).

[23]   E. A. Evans, R. Waugh, and L. Melnik, Biophysical Journal **16**, 585 (1976).

[24]   D. Carvajal, E. J. Laprade, K. J. Henderson, and K. R. Shull, Soft Matter **7**, 10508 (2011).

[25]   S. Knoche, D. Vella, E. Aumaitre, P. Degen, H. Rehage, P. Cicuta, and J. Kierfeld, Langmuir **29**, 12463 (2013).

[26]   E. Aumaitre, S. Knoche, P. Cicuta, and D. Vella, European Physical Journal E **36**, 22 (2013).

[27]   W. Yuan, E. J. Laprade, K. J. Henderson, and K. R. Shull, Soft Matter **10**, 1142 (2014).

[28]   F. Bashforth and J. C. Adams, (Camebridge University Press, 1883).

[29]   A. Yeung, T. Dabros, J. Masliyah, and J. Czarnecki, Colloids and Surfaces a-Physicochemical and Engineering Aspects **174**, 169 (2000).

[30]   D. Vella, A. Ajdari, A. Vaziri, and A. Boudaoud, Journal of the Royal Society Interface **9**, 448 (2012).

[31]   J. B. Segur and H. E. Oberstar, Industrial and Engineering Chemistry **43**, 2117 (1951).

[32]   *Physical Properties of Glycerine and Its Solutions* (Glycerine Producers' Association, New York, 1963).

[33]   C. Reichardt and T. Welton, *Solvents and Solvent Effects in Organic Chemistry* (Wiley-VCH, Weinheim, Germany, 2011), 4 edn.

[34]   W. Adamson and A. P. Gast, *Physical Chemistry of Surfaces* (John Wiley & Sons, New York, 1997), 6 edn.

[35]   C. W. Extrand and S. I. Moon, Langmuir **26**, 17090 (2010).

[36]   R. M. Prokop, M. L. Hair, and A. W. Neumann, Macromolecules **29**, 5902 (1996).

[37]   J. Zhu and R. C. Hayward, Journal of Colloid and Interface Science **365**, 275 (2012).

[38]   O. C. Farokhzad and R. Langer, Acs Nano **3**, 16 (2009).

[39]   B. Audoly and Y. Pomeau, *Elasticity and Geometry* (Oxford, New York, 2010).

[40]   M. Kraus, U. Seifert, and R. Lipowsky, Europhysics Letters **32**, 431 (1995).

[41]   S. Komura, K. Tamura, and T. Kato, European Physical Journal E **18**, 343 (2005).

[42]   T. Salez, M. Benzaquen, and E. Raphael, Soft Matter **9**, 10699 (2013).

[43]   A. Vaziri and L. Mahadevan, Proceedings of the National Academy of Sciences of the United States of America **105**, 7913 (2008).

[44]   L. Pauchard, Y. Pomeau, and S. Rica, Comptes Rendus De L Academie Des Sciences Serie Ii Fascicule B-Mecanique Physique Astronomie **324**, 411 (1997).

[45]   L. Pauchard and S. Rica, Philosophical Magazine B-Physics of Condensed Matter Statistical Mechanics Electronic Optical and Magnetic Properties **78**, 225 (1998).

[46]   M. P. Neubauer, M. Poehlmann, and A. Fery, Advances in Colloid and Interface Science **207**, 65 (2014).

[47]   S. Knoche and J. Kierfeld, Physical Review E **84**, 046608 (2011).

[48]   A. V. Pogorelov, *Bendings of Surfaces and Stability of Shells* (American Mathematical Society, Providence, RI, 1988).

[49]   L. D. Landau and E. M. Lifshitz, *Theory of Elasticity* (Pergamon Press, New York, 1975), 3 edn.

[50]   T. A. Witten, Reviews of Modern Physics **79**, 643 (2007).

[51]   M. E. R. Shanahan, Journal of Adhesion **79**, 881 (2003).

[52]   K. L. Johnson, *Contact Mechanics* (Cambridge University Press, New York, 2003).

[53]   D. J. Pochan, Z. Y. Chen, H. G. Cui, K. Hales, K. Qi, and K. L. Wooley, Science **306**, 94 (2004).

[54]   H. Cui, Z. Chen, S. Zhong, K. L. Wooley, and D. J. Pochan, Science **317**, 647 (2007).

[55]   A. P. Esser-Kahn, S. A. Odom, N. R. Sottos, S. R. White, and J. S. Moore, Macromolecules **44**, 5539 (2011).

[56]   C. Y. Lin and J. C. Slattery, Aiche Journal **28**, 147 (1982).

[57]   D. Platikanov, Journal of Physical Chemistry **68**, 3619 (1964).

[58]   K. Malysa, M. Krasowska, and M. Krzan, Advances in Colloid and Interface Science **114**, 205 (2005).

[59]   M. Krasowska and K. Malysa, Advances in Colloid and Interface Science **134-35**, 138 (2007).

[60]   L. Parkinson and J. Ralston, Journal of Physical Chemistry C **114**, 2273 (2010).

[61]   R. Manica and D. Y. C. Chan, Physical Chemistry Chemical Physics **13**, 1434 (2011).

[62]   K. Kumar, A. D. Nikolov, and D. T. Wasan, Journal of Colloid and Interface Science **256**, 194 (2002).

[63]   A. K. Malhotra and D. T. Wasan, Chemical Engineering Communications **48**, 35 (1986).

[64]   A. K. Malhotra and D. T. Wasan, Chemical Engineering Communications **55**, 95 (1987).

[65]   L. Y. Yeo, O. K. Matar, E. S. P. de Ortiz, and G. F. Hewitt, Journal of Colloid and Interface Science **241**, 233 (2001).

[66]   H. H. Shen and S. Hartland, Journal of Colloid and Interface Science **167**, 94 (1994).

[67]   R. Manica, J. N. Connor, R. R. Dagastine, S. L. Carnie, R. G. Horn, and D. Y. C. Chan, Physics of Fluids **20**, 032101 (2008).

[68]   S. Bekiranov, R. Bruinsma, and P. Pincus, Physical Review E **55**, 577 (1997).

[69]   D. H. Richards and M. Szwarc, Transactions of the Faraday Society **55**, 1644 (1959).

[70]   D. P. Rozairo and A. B. Croll, Langmuir **31**, 1303 (2015).

[71]   V. Mhetar and L. A. Archer, Macromolecules **31**, 8607 (1998).

[72]   Y. C. Jung and B. Bhushan, Journal of Physics-Condensed Matter **22**, 035104 (2010).

[73]   J. Ou, B. Perot, and J. P. Rothstein, Physics of Fluids **16**, 4635 (2004).

[74]   T. Kawakatsu, *Statistical Physics of Polymer* (Springer, Germany, 2004).

[75]   M. Doi and S. F. Edwards, *The theory of Polymer Dynamics* (Oxford Press, New York, NY, 1986).

[76]   R. A. L. Jones, *Soft Condensed Matter* (Oxford University Press, 2002), 1 edn.

[77]   W. C. Griffin, Journal of the Society of Cosmetic Chemists **1**, 311 (1946).

[78]   C.-S. Chern, *Principles and Applications of Emulsion Polymerization* (John Wiley & Sons, Inc, Hoboken, NJ, 2008).

[79]   A. F. M. Barton, *CRC Handbook of Solubility Parameters and Other Cohesion Parameters* (CRC Press, Boca Raton, FL, 1983).

[80]   I. Langmuir, Journal of the American Chemical Society **39**, 1848 (1917).

[81]   M. J. Rosen, *Surfactants and Interfacial Phenomena* (John Wiley & Sons, Inc, Canada, 1989), 2 edn.

[82]   I. Piirma, *Polymer Surfactants* (Marcel Decker, Inc, New York, NY, 1992).

[83]   S. Alexander, Journal De Physique **38**, 983 (1977).

[84]   P. G. Degennes, Journal De Physique **37**, 1445 (1976).

[85]   B. H. Cao and M. W. Kim, Faraday Discussions **98**, 245 (1994).

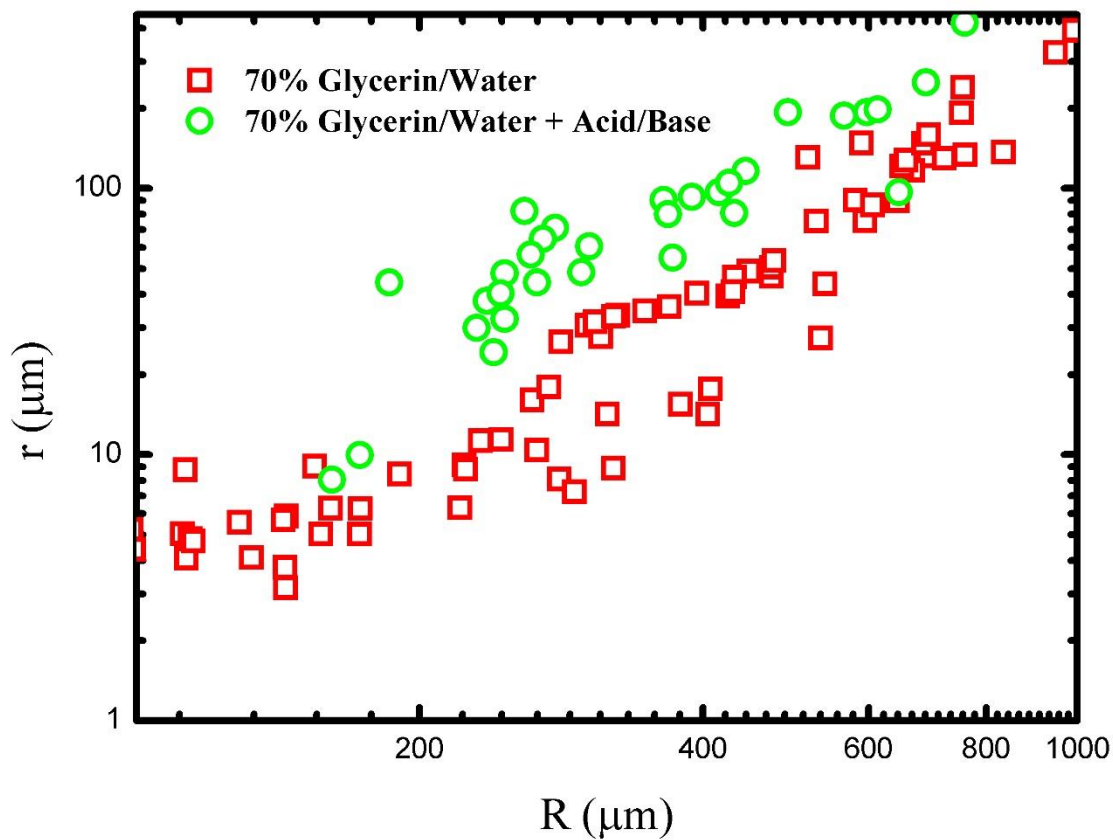[86]   N. C. Padmavathi and P. R. Chatterji, Langmuir **11**, 767 (1995).

Figure note: The elastic shell responded in a similar manner to both hydrochloric acid and pH 10 buffer solutions. Circular points show the response in the material in the presence of ionic liquid.

APPENDIX B. CALCULATION OF HEIGHT BY FITTING THE INTENSITY

The intensity at the center of a draining film was extracted. The circular points in figure 4.4(a) are experimentally extracted intensity over the period of drainage of the film. Using the maximas and the minimas, we can calculate the height (at the center of the draining film) at discrete points. The height over time is then fit with an exponential function. Although the height over time appear to be exponential, in reality a final thickness (minimum height) is reached within a finite time (instead of approaching zero at infinity as in an exponential function). Therefore, we use the full intensity data to calculate the height. The intensity we extract is the result of interference between the light rays reflected off of the mica surface and the drop surface. Therefore, we use

$$I = I_1^2 + I_2^2 + 2I_1I_2 \cos\left[\frac{4\pi h}{\lambda/i}\right]. \tag{B1}$$

to calculate the final intensity, using arbitrary values for I_1 and I_2. Here, λ is the wavelength of the laser beam (488 nm), i is the index of refraction of 60% glycerin in water and h is the height. A matlab code was used to iterate values of each height point and calculated the final fit intensity to match experimental intensity (within a certain error 'er'). The matlab code used to fit the intensity measurement, named 'heightgen' is as follows.

```
function []= heightgen(I1,I2,L,dh,er)
load height.txt
load intensity2.txt
h = height;
A = intensity2;
N = size(A);
tic
```

```
for i=N(1):-1:1

    h(i)=h(i)-0.05;

  C(i) = (I1*I1)+(I2*I2)+(2*I1*I2*cos(2*pi*h(i)/L));

  diff_1(i)= abs(C(i)-A(i));

   if diff_1(i) > er

      h(i) = h(i) + dh;

          C(i) = (I1*I1)+(I2*I2)+(2*I1*I2*cos(2*pi*h(i)/L));

          diff_2(i)= abs(C(i)-A(i));

        if diff_2(i) > diff_1(i)

             h(i)= h(i)-(dh*.01);

             C(i) = (I1*I1)+(I2*I2)+(2*I1*I2*cos(2*pi*h(i)/L));

             diff_2(i)= abs(C(i)-A(i));

           while diff_2(i) > er

             h(i) = h(i) - (dh*.01);

             C(i) = (I1*I1)+(I2*I2)+(2*I1*I2*cos(2*pi*h(i)/L));

             diff_2(i)= abs(C(i)-A(i));

           end

        else

          while diff_2(i) > er

             h(i) = h(i) + (dh);

             C(i) = (I1*I1)+(I2*I2)+(2*I1*I2*cos(2*pi*h(i)/L));

             diff_2(i)= (C(i)-A(i));
```

```
                end

            end

    else

    end

end


plot(C,'.')

hold all

plot(A,'.')

dlmwrite('Model_intensity',C)

dlmwrite('Model_height',h)

 toc
```